

A NEW OPTICAL SURVEY OF SUPERNOVA REMNANT CANDIDATES IN M31

Jong Hwan Lee¹ and Myung Gyoon Lee¹

¹*Astronomy Program, Department of Physics and Astronomy,
Seoul National University, Seoul 151-747, Republic of Korea*

leejh@astro.snu.ac.kr, mglee@astro.snu.ac.kr

ABSTRACT

We present a survey of optically emitting supernova remnants (SNRs) in M31 based on $H\alpha$ and [S II] images in the Local Group Survey. Using these images, we select objects that have $[S\ II]:H\alpha > 0.4$ and circular shapes. We find 76 new SNR candidates. We also inspect 234 SNR candidates presented in previous studies, finding that only 80 of them are SNR candidates according to our criteria. Combining them with the new candidates, we produce a master catalog of 156 SNR candidates in M31. We classify these SNR candidates according to two criteria: the SNR progenitor type [Type Ia and core-collapse (CC) SNRs] and the morphological type. Type Ia and CC SNR candidates make up 23% and 77%, respectively, of the total sample. Most of the CC SNR candidates are concentrated in the spiral arms, while the Type Ia SNR candidates are rather distributed over the entire galaxy, including the inner region. The CC SNR candidates are brighter in $H\alpha$ and [S II] than the Type Ia SNR candidates. We derive a cumulative size distribution of the SNR candidates, finding that the distribution of the candidates with $17 < D < 50$ pc is fitted well by a power law with the power law index $\alpha = 2.53 \pm 0.04$. This indicates that most of the SNR candidates identified in this study appear to be in the Sedov–Taylor phase. The $[S\ II]:H\alpha$ distribution of the SNR candidates is bimodal, with peaks at $[S\ II]:H\alpha \sim 0.4$ and ~ 0.9 . The properties of these SNR candidates vary little with the galactocentric distance. The $H\alpha$ and [S II] surface brightnesses show a good correlation with the X-ray luminosity of the SNR candidates that are center-bright. The SNR candidates with X-ray counterparts have higher surface brightnesses in $H\alpha$ and [S II] and smaller sizes than those without such counterparts.

Subject headings: galaxies: individual(M31) — galaxies:ISM — ISM:supernova remnants

1. INTRODUCTION

Supernova remnants (SNRs) play an important role in our understanding of supernovae (SNe), the interstellar medium (ISM), and the interaction between them. Large samples of SNRs in a galaxy can be used to understand the evolution of SNRs, estimate the SN rate in galaxies, and investigate the global properties of the ISM in the galaxy as well as the local ISM. SNRs are generally divided into two categories according to their progenitors: core-collapse (CC) and Type Ia SNRs. CC SNRs result from CC SNe caused by massive stars undergoing core collapse, while Type Ia SNRs are remnants of Type Ia SNe occurring when a white dwarf (WD) accretes material from its binary companion, causing the WD mass to exceed the Chandrasekhar limit. These two types of SNe eject different mixtures of heavy elements into the ISM of a galaxy, which have different impacts on the galactic chemical evolution. Therefore, a study of the properties of these two types of SNRs in galaxies can provide a clue to understand the star formation history and chemical evolution of galaxies.

There are 274 known SNR candidates in our Galaxy; thus, our Galaxy has the largest sample of known SNR candidates in the universe (Green 2009). However, they occupy too large an angular size in the sky and their distances are not well known, so it is difficult to obtain their optical properties. Therefore, the information on the statistical properties of these SNR candidates is very limited. On the other hand, SNR candidates in nearby galaxies do not suffer from these problems, so they are an ideal target for studying the optical properties statistically.

Extragalactic SNR surveys have been conducted at optical, radio, and X-ray wavelengths. The first SNR candidates were identified from a radio survey of the Large Magellanic Cloud (LMC) (Mathewson & Healey 1964). Since then, 77 SNR candidates have been identified in the MCs using radio, X-ray, and optical techniques (Filipović et al. 1998; Williams et al. 1999; Smith et al. 2000; van der Heyden et al. 2004; Payne et al. 2008; Badenes et al. 2010). However, limitations on the sensitivity and resolution reduce the effectiveness of radio and X-ray searches for SNRs in nearby galaxies. Therefore, optical searches have produced the largest number of extragalactic SNRs. Previous optical surveys identified ~ 230 SNR candidates in M31, ~ 140 SNR candidates in M33, and several hundred SNR candidates in other nearby galaxies using photometric and spectroscopic data (Magnier et al. 1995; Matonick & Fesen 1997; Matonick et al. 1997; Pannuti et al. 2002; Blair & Long 2004; Sonbas et al. 2009; Long et al. 2010; Dopita et al. 2010; Franchetti et al. 2012). Recently, Blair et al. (2012) found 225 SNR candidates in M83 using $H\alpha$ and $[S\ II]$ images obtained at the Magellan I 6.5 m telescope, and Leonidaki et al. (2013) identified ~ 400 SNR candidates in five nearby galaxies using narrow-band images obtained at the 1.4 m telescope.

However, SNR surveys in galaxies beyond the Local Group are limited by the available

sensitivity and resolution. Because SNRs in these galaxies are typically unresolved in ground-based images, their morphologies are largely unknown. Many of the previously known SNR candidates have sizes of $D > 100$ pc, which is larger than typical SNRs. Therefore, previous surveys might have included spurious SNRs such as H II regions and superbubbles. Additionally, they missed many faint and diffuse SNRs. Dopita et al. (2010) found 60 SNR candidates in M83 using high-resolution *HST* images, but they covered only a fraction of the galaxy.

We started a project to study SNRs in nearby galaxies using wide-field optical images. In this study, we selected M31, which is an appealing galaxy for studying SNRs owing to its proximity (~ 750 kpc, Vilardell et al. 2010; Riess et al. 2012). At the distance of M31, an SNR with $D \sim 20$ pc has an angular size of $\sim 5''$. Therefore, it is possible to distinguish many SNRs using ground-based images, characterize them in detail, and classify them considering their morphological structures. M31 has a significant number of optically identified SNRs. Dodorico et al. (1980) identified 19 SNR candidates on the basis of their [S II]:H α , and Blair et al. (1981) confirmed 14 SNR candidates with enhanced [S II]:H α using spectroscopic data. Braun & Walterbos (1993) found 52 SNR candidates using narrow-band images in H α and [S II], but their survey was limited to portions of the northwestern half of M31. Most of the known SNR candidates are credited to Magnier et al. (1995) who reported 179 SNR candidates. However, Magnier et al. (1995) did not cover the entire region of M31. They could not find faint SNRs because of the short exposure times. Additionally, because they used narrow-band images obtained under poor seeing conditions ($> 2''$), they could not resolve the SNRs well. For example, they could not distinguish SNRs located around the outside edges of giant H II regions. They included objects having large sizes ($D > 100$ pc), which might be superbubbles.

We conducted a new SNR survey of M31 using the data provided by the Local Group Survey (LGS) (Massey et al. 2006). M31 was observed as part of the LGS program with the KPNO/Mayall 4 m telescope in H α , [S II], and $\phi 3$ as well as other continuum bands. The survey covered the entire disk of M31. In this study, we present the results of the SNR survey over the entire disk region in M31. This paper is composed as follows. Section 2 describes the data and explains the methods used to identify SNR candidates, measure their sizes and fluxes, and classify them considering their progenitors and morphology. Section 3 provides a catalog of M31 SNR candidates and presents their spatial distributions, H α and [S II] luminosity functions, size distributions, [S II]:H α distributions, and radial distributions. In Section 4, we compare the optical properties of the M31 SNR candidates with those in other nearby galaxies, probe correlations between the optical properties and X-ray luminosity of the M31 SNR candidates, and investigate the difference between the distributions of Type Ia and CC SNR candidates. Finally, a summary and conclusion is given in Section 5.

2. DATA AND DATA REDUCTION

2.1. Data

We used the M31 images obtained from the LGS (Massey et al. 2006). It contains 10 overlapping fields across the disk of M31. Each field has an approximate angular size of $36' \times 36'$, and the entire survey covers 2.2 square degrees of M31. The pixel scale is $0.27''$ per pixel, with an average point spread function FWHM of $1''$. We used the images in $H\alpha$, [S II], and continuum bands that can be used to subtract most of the stellar emission. The $H\alpha$ filter is sufficiently broad to include some [N II] emission as well, but we will refer to it as the $H\alpha$ image.

2.2. Selection, Size Measurements, and Photometry of M31 SNR Candidates

We selected SNRs according to three criteria: [S II]: $H\alpha$, the morphology, and the absence of blue stars. [S II]: $H\alpha$ has often been used to distinguish SNRs from H II regions and planetary nebulae. SNRs typically have [S II]: $H\alpha > 0.4$, while H II regions and planetary nebulae have [S II]: $H\alpha \sim 0.1$ – 0.3 (Raymond 1979; Dopita et al. 1984; Levenson et al. 1995; Blair et al. 2012). To search for SNRs with enhanced [S II]: $H\alpha$, we prepared [S II]: $H\alpha$ images as follows. We used the R -band images to remove the continuum emission from the $H\alpha$ and [S II] images. We scaled the R -band images using scale factors determined from the magnitudes of bright stars and subtracted them from the corresponding $H\alpha$ and [S II] images. Then we made [S II]: $H\alpha$ images from these continuum-subtracted $H\alpha$ and [S II] images. To identify SNRs, we visually inspected the continuum-subtracted $H\alpha$ and [S II] images and [S II]: $H\alpha$ images. We searched for round or shell-like objects bright in both the $H\alpha$ and [S II] images with [S II]: $H\alpha > 0.4$ in the [S II]: $H\alpha$ images. We checked for the presence of blue stars inside the selected objects using the B -band images and rejected the objects that contained blue stars inside. The rejected objects may be H II regions or superbubbles. In some SNR candidates with partial shells, a few blue stars were found in the region of little [S II] emission. We kept these objects as SNR candidates. Thus, we selected 354 SNR candidates in the first step.

To choose the SNRs from among these candidates, we derived an integrated [S II]: $H\alpha$ for each SNR candidate. To measure their fluxes, we defined their sizes using [S II]: $H\alpha$ images. Because most of them have circular shapes, we estimated the sizes of the circles defined by the region with [S II]: $H\alpha > 0.4$. When only a partial shell is visible, we estimated its size from the curvature of the visible portion. Then we conducted aperture photometry of the continuum-subtracted $H\alpha$ and [S II] images to extract the flux within the circular regions defined above.

In a few instances where a nearby bright star was poorly subtracted, we masked out that region. We derived the integrated [S II]:H α from the H α and [S II] fluxes for the 354 SNR candidates. Finally, we selected 156 objects with integrated [S II]:H α > 0.4 among the SNR candidates. Of these, 76 are new SNR candidates, and 80 were listed in previous studies (Dodorico et al. 1980; Blair et al. 1981; Braun & Walterbos 1993; Magnier et al. 1995).

The most extensive survey of M31 SNR candidates in previous studies was that of Magnier et al. (1995). They presented a list of 179 SNR candidates they found using H α , [S II], and *V*-band images. They divided their sample into three categories according to the confidence level: 14 with the highest confidence, 54 with moderate confidence, and 111 with the lowest confidence. They also listed 55 SNR candidates found by other authors (Dodorico et al. 1980; Blair et al. 1981; Braun & Walterbos 1993). We inspected these 234 SNR candidates using the LGS data. We examined whether the SNR candidates have [S II]:H α > 0.4 and whether blue stars exist inside the objects. We consider 154 of these objects to non-SNRs. They may be H II regions, superbubbles, or diffuse ionized gas. Of these, 93 SNR candidates have [S II]:H α < 0.4 and contain blue stars inside, so they are likely H II regions. Another 13 of the candidates have slightly larger values of $0.4 < [\text{S II}]:\text{H}\alpha < 0.6$ but contain blue stars inside. Therefore, they are also probably H II regions. Another 44 of the candidates are larger than $D = 100$ pc and contain a number of blue stars inside. They are probably superbubbles. Finally, 4 of the candidates have high values of [S II]:H α > 0.8 but show very low surface brightnesses. We consider them to be diffuse ionized gas. We present a catalog of SNR candidates rejected according to our criteria in Table 1. The fractions of our SNR candidates matched with previous studies are $\sim 64\%$ (9 of 14), $\sim 28\%$ (15 of 54), and $\sim 22\%$ (24 of 111) for the highest, moderate, and lowest confidence category, respectively, in Magnier et al. (1995), and $\sim 58\%$ (32 of 55) for the other SNR candidates (Dodorico et al. 1980; Blair et al. 1981; Braun & Walterbos 1993). In summary, we found that only 80 of the 234 known SNR candidates are SNRs according to our criteria.

Figure 1 shows the positions of the 76 new SNR candidates as well as the 80 known SNR candidates in M31. Some of the new SNR candidates are located outside the survey region of Magnier et al. (1995), and some faint SNR candidates not cataloged in Magnier et al. (1995) were detected because deeper images were used in this study. The positions of the SNR candidates are displayed on a gray-scale map of the *Spitzer* MIPS 24 μm band image, which clearly shows the star-forming regions in the spiral arms and ring structures at 5, 12, and 15 kpc (Gordon et al. 2006). Most of the M31 SNR candidates are concentrated in the spiral arms and three ring structures.

In Figure 2, we compare the sizes of the SNR candidates common to this study and Magnier et al. (1995) (scaled for a distance of 750 kpc). It shows a good correlation between

the two measurements, but with an offset. A linear least-squares fit to the data produces $D(\text{this study}) = 1.07(\pm 0.08) \times D(\text{Magnier et al. 1995}) + 4.2(\pm 3.4) \text{ pc}$. The offset indicates that the measurements of Magnier et al. (1995) are, on average, smaller than ours by approximately $1''$.

2.3. Classification of SNR Progenitors

The progenitors of CC SNe are massive stars associated with star-forming regions, while those of Type Ia SNe are white dwarfs that belong to Population II. Therefore, the properties of the stellar and interstellar populations in and around SNRs have been used to determine the types of their progenitor SNe (Chu & Kennicutt 1988; Badenes et al. 2009; Franchetti et al. 2012; Jennings et al. 2012). For instance, a lack of nearby massive stars or H II regions around an SNR suggests that it may have originated from a white dwarf binary, while the presence of nearby massive stars or H II regions suggests that it is probably a descendant of a CC SN.

We attempted to classify the progenitor types of our SNR candidates as Type Ia SNe and CC SNe according to the presence of OB stars or H II regions. First, we obtained the B and V magnitudes of the stars in M31 given by Massey et al. (2006). Among the bright stars with $V < 22 \text{ mag}$ ($M_V < -2.6 \text{ mag}$), we considered the blue stars with $B - V < 0$ [$(B - V)_0 < -0.06$ for $E(B - V) = 0.06$] to be OB stars. We counted the OB stars located between the boundary of each SNR candidate and 100 pc from the center of each SNR candidate, $N(\text{OB})$, following Chu & Kennicutt (1988) and Franchetti et al. (2012). For the SNR candidates in the LMC, $N(\text{OB})$ for most of the Type Ia SNR candidates is smaller than two (Chu & Kennicutt 1988). Second, we used a catalog of M31 H II regions based on $\text{H}\alpha$ images in the LGS (J. H. Lee & M. G. Lee 2014, in preparation). We counted the H II regions with $L > 10^{36} \text{ erg s}^{-1}$ located between the boundary of each SNR candidate and 100 pc from the center of each SNR candidate, $N(\text{HII})$. In this study, we considered the objects with $N(\text{OB}) > 1$ or $N(\text{HII}) > 1$ to be CC SNR candidates.

2.4. Classification of SNR Morphology

The Milky Way (MW) SNRs show various morphologies in the radio: shell (78%), composite (12%), and filled-center (4%) remnants (Green 2009). For example, Cas A has a nearly complete shell, and the Cygnus Loop is circular in shape except for a break-out toward the south. However, the Crab Nebula consists of a broadly oval-shaped mass of filaments

surrounding a diffuse blue central region. We examined the morphology of the 156 SNR candidates in M31 and recognized that they also have various shapes. The morphological features seen in these SNR candidates include a discrete shell and a center-bright nebula or diffuse nebula. They are located in various environments. Some are isolated objects, while some lie on or within H II regions near the star-forming regions.

We therefore attempted to group the SNR candidates considering their optical morphology and general environments. SNRs beyond the Local Group are typically unresolved in ground-based images, but most of those in M31 are resolved even in the LGS data. Therefore, it is possible to classify these SNR candidates into several groups using the classification criteria summarized in Table 2. In Figure 3, we show typical examples of SNR candidates of different morphological types in continuum-subtracted $H\alpha$ and [S II] images.

We classified the morphology of the SNR candidates as follows: (a) A-type SNR candidates having well-defined, nearly complete shells; (b) B-type SNR candidates showing partial shells; and (c) C-type SNR candidates, which are poorly defined objects. As a pragmatic distinction, we defined A1-type SNR candidates as objects showing well-formed, limb-brightened, and nearly complete shells. We defined A2-type SNR candidates as compact and center-bright objects that may not show a shell structure but are nevertheless clearly defined. A3-type SNR candidates show nearly circular shapes but do not have distinct limb-brightened shells. They show more diffuse and faint emission in [S II] than A1-type or A2-type SNR candidates.

We defined B1-type SNR candidates as objects having limb-brightened partial shells. Fainter patchy and diffuse emission fills the interior of the partial shells. B2-type SNR candidates have partial shells, and they are patchy and ill-defined SNR candidates embedded in star-forming regions. However, they are easily distinguished from other objects in the [S II] images. In terms of environment, B2-type SNR candidates are located within nebosity, and most of them are in spiral arms. The objects except for the B2-type SNR candidates are isolated from other nebosity. B3-type SNR candidates have faint and diffuse emission in [S II] and partial shells with lower surface brightness than B1-type SNR candidates. B4-type SNR candidates have faint emission with modest brightening on one side. They have higher [S II]: $H\alpha$ than B3-type SNR candidates. C-type SNR candidates include ambiguous objects, excluding A-type and B-type SNR candidates. Eight of them are center-bright objects having a small size ($D < 20$ pc) and low $H\alpha$ luminosity. A2-type SNR candidates and small C-type SNR candidates ($D < 20$ pc) correspond to composite or filled-center remnants in the MW, and the rest correspond to shell remnants in the MW.

3. RESULTS

3.1. A Catalog of M31 SNR Candidates

We present a catalog of the 156 SNR candidates selected from $H\alpha$ and $[S\ II]$ images in Table 3. Table 3 lists their positions, $H\alpha$ and $[S\ II]$ luminosities, sizes, $[S\ II]:H\alpha$, morphological types, numbers of OB stars and H II regions around the SNR candidates, progenitor types, and other names in previous studies. Forty-two of the total sample more likely result from Type Ia SNe, with the remainder more likely to be from CC SNe. Thus, the number ratio of Type Ia SNR candidates and CC SNR candidates is $\sim 1:3$. The numbers of A-type, B-type, and C-type SNR candidates are 54, 85, and 17, respectively. The fractions of Type Ia SNR candidates are $\sim 30\%$ and $\sim 27\%$ for A-type and B-type SNR candidates, respectively. The fractions of Type Ia SNR candidates are especially high for A2-type ($\sim 40\%$) and B4-type SNR candidates ($\sim 53\%$). The numbers of SNR candidates with shells (or partial shells) and center-bright structure are 133 ($\sim 85\%$) and 23 ($\sim 15\%$), respectively. These fractions are comparable to those for the MW SNRs.

Figure 4 plots the distributions of the $H\alpha$ and $[S\ II]$ surface brightnesses of the A-type and B-type SNR candidates. Most of the A-type SNR candidates have higher surface brightnesses than the B-type SNR candidates. The A2-type SNR candidates have high luminosities and small sizes, and they are center-bright objects. Therefore, they have higher $H\alpha$ and $[S\ II]$ surface brightnesses than A1-type SNR candidates, which have complete shells. The B2-type SNR candidates have higher $H\alpha$ and $[S\ II]$ surface brightnesses than the other B-type SNR candidates. This is because most of them are located in star-forming regions that have a higher ISM density.

3.2. Spatial Distributions of M31 SNR Candidates

Figures 5(a) and (b) display the spatial distributions of the 42 Type Ia and 114 CC SNR candidates in the sky and in the deprojected coordinates, respectively. For deprojection, we set the position angle of the major axis as 37.7° and the inclination angle as 77.5° (de Vaucouleurs 1958). Most of the CC SNR candidates are concentrated in the spiral arms, while the Type Ia SNR candidates are rather spread over the entire galaxy, including the inner region.

We plot, in Figure 6, the radial distributions of the number density for all, CC, and Type Ia SNR candidates in M31. The distribution of all the SNR candidates shows a dominant peak at the deprojected galactocentric distance (R) of 12 kpc and a much weaker peak

at $R \sim 5$ kpc. The distribution of the CC SNR candidates is similar to that of all the SNR candidates, showing two distinct peaks at $R \sim 5$ kpc and ~ 12 kpc. In contrast, the distribution of the Type Ia SNR candidates is broad, showing no distinct peaks. These results show clearly that the CC SNR candidates are strongly correlated with star-forming regions, while the Type Ia SNR candidates are not. Note that there is one isolated SNR candidate in the southeast, ~ 1.8 deg from the center of M31: ID number 1. Its progenitor type is Type Ia, and its morphological type is B4. Its size is 47 pc, and its $H\alpha$ luminosity is $10^{35.72}$ erg s $^{-1}$.

Figure 7 displays the radial distributions of the number density for all, A-type, and B-type SNR candidates in M31. Most of the SNR candidates at $R < 7$ kpc are A-type SNR candidates, while there are more B-type SNR candidates in the outer region at $R > 7$ kpc. The morphology of an SNR depends on the distribution of the ambient medium. SNRs expanding into a uniform ambient ISM are expected to have a more complete shell structure. Therefore, the radial distribution of A-type SNR candidates indicates that the ISM at $R < 7$ kpc may be more uniform than that in the outer regions.

3.3. $H\alpha$ and [S II] Luminosity Functions of M31 SNR Candidates

Figures 8(a) and (b) plot the $H\alpha$ and [S II] luminosity functions, respectively, of all, CC, and Type Ia SNR candidates in M31. The $H\alpha$ luminosity of all the SNR candidates ranges from $L(H\alpha) = 10^{34.8}$ erg s $^{-1}$ to $10^{37.2}$ erg s $^{-1}$, and their [S II] luminosity ranges from $L([S II]) = 10^{34.6}$ erg s $^{-1}$ to 10^{37} erg s $^{-1}$. The lower limits of the $H\alpha$ and [S II] luminosities are determined by the observational threshold on the surface brightness. The Type Ia SNR candidates have $H\alpha$ luminosities ranging from $L(H\alpha) = 10^{35.6}$ erg s $^{-1}$ to $10^{36.6}$ erg s $^{-1}$, and they are typically fainter than the CC SNR candidates.

We used a double power law function to fit the bright part of the $H\alpha$ luminosity function:

$$N(L)dL = AL^{\alpha_1}dL \quad \text{for } L \geq L_b,$$

and

$$N(L)dL = A'L^{\alpha_2}dL \quad \text{for } L < L_b,$$

where L_b is the break-point luminosity ($10^{36.6}$ erg s $^{-1}$), and $A' = AL_b^{(\alpha_2 - \alpha_1)}$. For the bright part, we obtained a power law index of $\alpha = -2.61 \pm 0.42$. For the faint part, the $H\alpha$ luminosity function becomes much flatter than that for the bright part, with $\alpha = -1.26 \pm 0.17$. On the other hand, the bright part of the [S II] luminosity function is fitted by a single power law with an index of $\alpha = -2.24 \pm 0.03$.

3.4. Size Distributions of M31 SNR Candidates

Figure 9(a) displays the differential size distributions of all, CC, and Type Ia SNR candidates in M31. The size of all the SNR candidates ranges from 8 pc to 100 pc, and most of them have sizes of $20 \text{ pc} < D < 60 \text{ pc}$. The size distribution of all the candidates shows a strong peak at $D \sim 48 \text{ pc}$ with a broad wing. This indicates that our sample appears to be incomplete for $D > 48 \text{ pc}$. The size distribution of the CC SNR candidates shows a strong peak at $D \sim 48 \text{ pc}$, while that of the Type Ia SNR candidates is much broader, with a weak peak at $D \sim 40 \text{ pc}$. Most of the small SNR candidates with $D < 25 \text{ pc}$ are CC SNR candidates.

It is well known that the cumulative size distribution of SNRs in a galaxy is useful for understanding the evolution of an SNR, and it is often fitted with a power law (Mathewson et al. 1983; Gordon et al. 1998; Bandiera & Petruk 2010; Dopita et al. 2010; Badenes et al. 2010). According to the classical theory, an SNR evolves through four different phases in its passage to the point where it merges with the ambient ISM (Woltjer 1972; McKee & Ostriker 1977; Dopita & Sutherland 2003; Draine 2011). In the free expansion phase, SN ejecta sweep up ambient ISM as the SNR expands freely ($D \propto t$). When sufficient masses of the ISM have been swept up, the SNR expands adiabatically in a Sedov–Taylor phase ($D \propto t^{2/5}$). During the Sedov–Taylor phase, the SNR is most likely to be observed at X-ray or radio wavelengths.

A radiative phase ($D \propto t^{2/7}$) occurs when the forward shock becomes sufficiently slow and old to start radiating the energy stored in the hot gas. Most SNRs in this phase are seen at optical wavelengths. Finally, the SNR enters a snowplow phase ($D \propto t^{1/4}$) before it merges with the general ISM. Supposing a constant SN rate in a galaxy, we would expect the cumulative size distribution of SNRs to become steeper as SNRs evolve, following $N(< D) \propto D$, $N(< D) \propto D^{2.5}$, and $N(< D) \propto D^{3.5}$ in the free expansion, Sedov–Taylor, and radiative phases, respectively. The sizes at which the transitions among these three phases occur can be related to the SN ejecta mass, SN explosion energy, and ambient density (Blondin et al. 1998; Truelove & McKee 1999).

Figure 9(b) plots the cumulative size distributions of all, CC, and Type Ia SNR candidates in M31. The distribution of all the SNR candidates is well represented by power law forms, showing two break points at $D = 17 \text{ pc}$ and 50 pc . The slopes are $\alpha = 1.65 \pm 0.02$ for $D < 17 \text{ pc}$ and $\alpha = 2.53 \pm 0.04$ for $17 \text{ pc} < D < 50 \text{ pc}$, respectively. Considering the above theory, the small SNR candidates with $D < 17 \text{ pc}$ might be in the free expansion phase, while the large SNR candidates with $17 \text{ pc} < D < 50 \text{ pc}$ might be in the Sedov–Taylor phase. Thus, most of the M31 SNR candidates found in this study appear to be in the Sedov–Taylor phase. The slopes for the CC and Type Ia SNR candidates are similar to that for all the SNR candidates, $\alpha = 2.30 \pm 0.04$ for $15 \text{ pc} < D < 55 \text{ pc}$ and $\alpha = 2.45 \pm 0.06$ for $25 \text{ pc} < D <$

50 pc, respectively. The difference in size ranges between the two types of SNR candidates indicates that most of the CC SNR candidates may lie in a denser ambient ISM than the Type Ia SNR candidates.

Figures 10(a) and (b) display the differential and cumulative size distributions, respectively, of all, A-type, B-type, and C-type SNR candidates. The A-type SNR candidates have a nearly flat distribution from $D = 20$ pc to $D = 50$ pc, while the distribution of B-type SNR candidates shows a broad peak at $D \sim 55$ pc. The mean size of the A-type SNR candidates is $D \sim 35$ pc, which is much smaller than that of the B-type SNR candidates, $D \sim 60$ pc. In Figure 10(b), the slopes for the A-type and B-type SNR candidates are $\alpha = 2.15 \pm 0.09$ for $25 \text{ pc} < D < 45 \text{ pc}$ and $\alpha = 4.63 \pm 0.14$ for $35 \text{ pc} < D < 60 \text{ pc}$, respectively. This indicates that B-type SNR candidates may evolve faster than A-type SNR candidates.

3.5. [S II]:H α Distributions of M31 SNR Candidates

Figure 11(a) shows the [S II]:H α distributions of all SNR candidates, new SNR candidates, and known SNR candidates presented in previous studies. The [S II]:H α distribution of all the SNR candidates is bimodal, with peaks at [S II]:H $\alpha \sim 0.4$ and ~ 0.9 . The SNR candidates identified in previous studies have [S II]:H α values ranging from 0.4 to 1.2, with a strong peak at [S II]:H $\alpha \sim 0.4$. The new SNR candidates have [S II]:H α values ranging from 0.4 to 1.8, and their [S II]:H α distribution is nearly uniform in the range of $0.4 < [\text{S II}]:\text{H}\alpha < 1.4$. Note that a few of the new SNR candidates have high values of [S II]:H $\alpha > 1.4$. Figure 11(b) plots the [S II]:H α distributions of all, CC, and Type Ia SNR candidates. Both the CC and Type Ia SNR candidates have similar ranges of [S II]:H α . The [S II]:H α distributions of the CC and Type Ia SNR candidates are similarly bimodal. The number ratio of CC SNR candidates and Type Ia SNR candidates is higher for low [S II]:H α than for high [S II]:H α . Therefore, SNR candidates can be divided into two groups: a low [S II]:H α group and a high [S II]:H α group. This division depends on the morphological type.

Figure 12 displays the [S II]:H α distributions of M31 SNR candidates of various morphological types. The [S II]:H α distributions are separated into two groups at the boundary of [S II]:H $\alpha \sim 0.8$. The high [S II]:H α populations are mostly A1-type, A2-type, B1-type, and B4-type SNR candidates that have well-defined shell-like or compact shapes, while the low [S II]:H α populations are mostly A3-type and B3-type SNR candidates that have low surface brightnesses and smooth shapes. Additionally, B2-type SNR candidates are embedded in star-forming regions, and they have high H α luminosity and low [S II]:H α .

3.6. Radial Variation in Physical Properties of M31 SNR Candidates

Figure 13 shows the (a) $H\alpha$ luminosity, (b) [S II] luminosity, (c) size, (d) $H\alpha$ surface brightness, and (e) [S II] surface brightness of the M31 SNR candidates as a function of R . In each panel, the star symbols indicate the mean values in a distance bin of 2 kpc. The vertical error bars denote the standard deviations of the values in the distance bin. Most of the SNR candidates are concentrated at $R \sim 12$ kpc, which corresponds approximately to a well-known star-forming ring (Gordon et al. 2006). The radial variations in the $H\alpha$ and [S II] luminosities of the SNR candidates are negligible. In the inner region ($R < 10$ kpc), the mean size of the SNR candidates increases from 40 pc to 60 pc as R increases, while the mean values of their $H\alpha$ and [S II] surface brightnesses decrease. Beyond 10 kpc, no radial trend appears. Thus, there are compact SNR candidates with smaller sizes and higher $H\alpha$ and [S II] surface brightnesses in the inner region of M31. We inspected the radial variations in the physical properties of the M31 SNR candidates according to their morphology and found little radial variation in the properties of SNR candidates of different morphological types.

Figure 14 shows the radial variation in [S II]: $H\alpha$ for the M31 SNR candidates. Although [S II]: $H\alpha$ cannot be used to determine the abundances without an analysis of the ionization conditions, radial gradients in [S II]: $H\alpha$ for SNRs are often seen (Blair & Long 1997; Galarza et al. 1999; Blair & Long 2004). In Figure 14, we compare the radial distribution of [S II]: $H\alpha$ for the M31 SNR candidates identified in this study with that for the M31 SNR candidates presented by Galarza et al. (1999). Galarza et al. (1999) presented the radial variation in [S II]: $H\alpha$ for 22 SNR candidates in M31 on the basis of spectroscopic data indicating that [S II]: $H\alpha$ decreases from the center of the galaxy outward. They suggested that this trend is a direct result of an abundance gradient in M31. In contrast, the [S II]: $H\alpha$ of a much larger sample of all SNR candidates in this study shows a large scatter and little variation with R . Similar results are seen for the SNR candidates of different morphological types. Note, however, that only SNR candidates with a high [S II]: $H\alpha$ (> 0.8) are found in the inner region ($R < 6$ kpc).

3.7. Luminosity–Size Relation and Surface Brightness–Size Relation for M31 SNR Candidates

We inspected the relations among the luminosity, size, and surface brightness of all, Type Ia, and CC SNR candidates in M31, and the results are summarized in Table 4. Figures 15(a) and (b) display the luminosity versus size for Type Ia and CC SNR candidates in M31. The $H\alpha$ and [S II] luminosities of all the M31 SNR candidates show weak linear correlations with their sizes. The $H\alpha$ and [S II] luminosities of the CC SNR candidates show

linear correlations with their sizes, while those of the Type Ia SNR candidates show little correlation. The relations for the CC SNR candidates excluding C-type SNR candidates are fitted by $L \propto D^{2.49 \pm 0.20}$ and $L \propto D^{2.22 \pm 0.18}$ in $H\alpha$ and $[S\ II]$, respectively. Thus, the larger CC SNR candidates are, the brighter they are.

The relation between the surface brightness Σ and size D ($\Sigma - D$ relation) for SNRs has been used to estimate the distances to the MW SNRs (Pavlović et al. 2013). The $\Sigma - D$ relation for SNRs is often given as

$$\Sigma(D) = AD^{-\beta},$$

where A and the slope β are obtained by fitting the observational data for a sample of SNRs. In Figures 15(c) and (d), the $H\alpha$ and $[S\ II]$ surface brightnesses of the M31 SNR candidates, excluding C-type SNR candidates, show weak linear correlations with their sizes. The $H\alpha$ and $[S\ II]$ surface brightnesses of the Type Ia SNR candidates show stronger linear correlations with their sizes than the CC SNR candidates. The slopes for the $\Sigma - D$ relation in $H\alpha$ and $[S\ II]$ for the Type Ia SNR candidates, excluding C-type SNR candidates, are $\beta = 2.40 \pm 0.24$ and $\beta = 2.42 \pm 0.30$, respectively. Larger Type Ia SNR candidates tend to have lower surface brightness.

Figure 16 displays the luminosity versus the size of the M31 SNR candidates of different morphological types. Note that the $H\alpha$ and $[S\ II]$ luminosities of each morphological type show tight linear correlations with the sizes. Table 5 lists the fitting results for the relations between the properties of the SNR candidates. The relation between the size and $H\alpha$ luminosity of A1-type SNR candidates is fitted by $L \propto D^{2.13 \pm 0.22}$. The SNR candidates with other morphological types yield similar indices: from 1.89 ± 0.12 for B4-type SNR candidates to 2.34 ± 0.19 for B2-type SNR candidates. An exception is A3-type SNR candidates, which show 1.53 ± 0.29 . The indices for the correlations between the size and $[S\ II]$ luminosity are similar to those for the correlations between the size and $H\alpha$ luminosity. Figure 17 shows the distributions of the $H\alpha$ and $[S\ II]$ surface brightnesses with respect to the sizes of the M31 SNR candidates. Only A2-type and A3-type SNR candidates show linear correlations between the surface brightness and size: $\beta(H\alpha) = 1.32 \pm 0.29$ and 1.19 ± 0.14 for A2-type and A3-type SNR candidates, and $\beta([S\ II]) = 1.50 \pm 0.32$ and 1.24 ± 0.18 for A2-type and A3-type SNR candidates, respectively.

4. DISCUSSION

4.1. Selection Effects, Biases, and Completeness

Optical SNR surveys suffer from incompleteness in the large and small SNRs (Matonick & Fesen 1997; Matonick et al. 1997; Gordon et al. 1998). Large SNRs are hard to identify because of their low surface brightness, and small SNRs are difficult to distinguish because of confusion with other sources. The background surface brightness is higher in star-forming regions than in quiet regions, so the detection of large SNRs with low surface brightness will be more difficult in star-forming regions. Crowding of emission line objects is more severe in star-forming regions than in quiet regions, so the detection of small SNRs will be more difficult when their sizes are similar to those of point sources.

We discuss these problems in our survey of SNR candidates. We selected SNR candidates larger than $2''$ ($D \sim 7.2$ pc), which is twice the size of the point sources ($\text{FWHM} \sim 1''$) in the images we used. Note that the LGS images we used were obtained under seeing conditions twice as good as those used in previous studies (Magnier et al. 1995). The size distribution of the SNR candidates in Figure 9 shows that the number of SNR candidates decreases abruptly at $D = 17$ pc as the size of the candidates decreases and that only a few candidates have sizes of $D = 8 - 17$ pc. This indicates three things. First, a few small SNR candidates were missed in the star-forming regions owing to the confusion problem in our survey. Second, we might have missed young Balmer-line-dominated SNRs that exhibit little $[\text{S II}]:\text{H}\alpha$ enhancement (Smith et al. 1991). Third, there is a minimum size for which our methodology was able to identify optical SNR candidates in M31, which is about 17 pc. This corresponds to the transition stage from the free expansion phase to the Sedov–Taylor phase.

We used an $\text{H}\alpha$ and $[\text{S II}]$ surface brightness limit of $10^{-16.5}$ erg cm $^{-2}$ s $^{-1}$ arcsec $^{-2}$ and a maximum size limit of $D \sim 100$ pc for SNR detection. The surface brightness of SNRs decreases as they expand. The $\log SB(\text{H}\alpha)$ versus $\log D$ diagram in Figure 15 shows a few notable points in this regard. First, the surface brightness of the SNR candidates in our sample decreases as they become larger, as expected. Second, the number of CC SNR candidates is smaller than that of Type Ia SNR candidates at low surface brightness ($-16.5 < \log SB < -16.0$, which corresponds to a size range of $D = 50$ pc to 100 pc). Most of the former are located in the star-forming region, while the latter are in the quieter region. This indicates that fewer SNR candidates larger than $D = 50$ pc might have been detected in the star-forming regions. However, the completeness of the SNR candidates smaller than $D = 50$ pc must be high. We determined the slope of the cumulative size distribution of the SNR candidates using only the data for $17 \text{ pc} < D < 50 \text{ pc}$ so that the fitting result will be affected little by incompleteness.

4.2. Comparison of the Physical Properties of SNR Candidates in M31 and Other Nearby Galaxies

We compared the physical properties of M31 SNR candidates with those of candidates in the MCs and M33. Mathewson et al. (1983) first presented a catalog of 31 SNR candidates in the MCs obtained from X-ray, radio, and optical images. Since then, there have been numerous MC SNR searches using multiwavelength data (Filipović et al. 1998; Williams et al. 1999; Filipović et al. 2005; van der Heyden et al. 2004; Payne et al. 2008). At optical wavelengths, Smith et al. (2000) performed the Magellanic Clouds Emission Line Survey, which covered most regions of the MC with $H\alpha$, $[S II]$, and $\phi 3$ images and identified SNR candidates with high $[S II]:H\alpha$. However, the results of this survey are not yet published. Instead, Badenes et al. (2010) introduced a merged catalog of SNR candidates confirmed in previous studies. This catalog includes the position, size, and radio flux of 54 and 23 SNR candidates in the LMC and SMC, respectively.

Dodorico et al. (1978) identified 3 SNR candidates in M33. Subsequent studies have increased the number of optically selected SNR candidates to nearly 100 (Dodorico et al. 1980; Long et al. 1990; Gordon et al. 1998). Long et al. (1996) found X-ray counterparts to 10 optically identified SNR candidates. Since then, other authors have identified new SNR candidates using *XMM–Newton* and *Chandra* (Pietsch et al. 2004; Ghavamian et al. 2005; Misanovic et al. 2006; Gaetz et al. 2007; Plucinsky et al. 2008). Most recently, Long et al. (2010) presented a catalog of 137 SNR candidates, 82 of which were detected in *Chandra* data.

Figure 18(a) compares the $H\alpha$ luminosity function of the M31 SNR candidates in this study with that of the M33 SNR candidates (Long et al. 2010). Both the M31 and M33 SNR candidates were detected to nearly the same limit. There are more M31 SNR candidates at the faint part of the luminosity function but more M33 SNR candidates at the bright part. Figure 18(b) compares the $H\alpha$ surface brightnesses of the M31 and M33 SNR candidates. The ranges of $H\alpha$ surface brightness are also nearly the same. Similar to the case for the $H\alpha$ luminosity, the M31 SNR candidates have lower surface brightness than the M33 SNR candidates. These results indicate that most of the M31 SNR candidates may lie in a less dense ambient ISM than the M33 SNR candidates. Alternatively, the SNR search for M33 might have missed faint and diffuse SNRs and might have included H II regions or superbubbles that have high $H\alpha$ luminosities and OB stars in nebulae.

Figure 18(c) shows the differential size distributions of SNR candidates in M31, M33, the LMC, and the SMC. The sizes of the SNR candidates in M33 and the MCs were obtained from Long et al. (2010) and Badenes et al. (2010), respectively. The MC SNR candidates have sizes from 0.5 pc (SNR 1987A) to ~ 160 pc (DEM L203), and the M33 SNR candidates

have sizes that range from 8 pc (L10-028) to 179 pc (L10-080). However, the range of sizes for the M31 SNR candidates is narrower than that for the MCs and M33. The objects with $D > 100$ pc among the SNR candidates in the MCs and M33 may be superbubbles. The size distributions of the SNR candidates vary depending on the galaxy. The distribution of the M31 SNR candidates shows a narrow peak at $D \sim 45$ pc, while that of the M33 SNR candidates shows a broader peak at $D \sim 40$ pc. On the other hand, the size distributions of the SNR candidates in the MCs have a broad peak at smaller size, $D \sim 25$ pc.

4.3. Comparison of Cumulative Size Distributions of SNR Candidates in M31 and Other Nearby Galaxies

The cumulative size distributions of SNRs in nearby galaxies has long been a topic of study, and they are often represented by power law forms (Mathewson et al. 1983; Mills et al. 1984; Green 1984; Hughes & Helfand 1984; Long et al. 1990; Gordon et al. 1998; Dopita et al. 2010; Badenes et al. 2010). Mathewson et al. (1983) presented the cumulative size distribution of 21 CC SNR candidates with $D < 50$ pc in the LMC, and the distribution is well fitted by a power law with an index $\alpha = 1.0 \pm 0.2$. They interpreted the shape of the size distribution as evidence that most of the MC SNR candidates are in the free expansion phase. Mills et al. (1984) showed that a power law index for the cumulative size distribution of the 24 SNR candidates with $7 \text{ pc} < D < 40 \text{ pc}$ in the MW is $\alpha = 1.2 \pm 0.36$, and they suggested that the MW SNR candidates are also in the free expansion phase. Long et al. (1990) identified 30 SNR candidates in M33 using optical narrow-band images, and they showed that the cumulative size distribution of 21 SNR candidates with $D < 30$ pc is represented by a power law with an index of $\alpha = 2.1$. They suggested that most of the M33 SNR candidates are in the Sedov–Taylor phase. However, these results were somewhat affected by incompleteness of the SNR samples.

Figure 19 compares the cumulative size distribution of the M31 SNR candidates with those of the candidates in M33, the MCs, and the MW. We derived the cumulative size distributions using larger samples than those found in previous studies. The distributions are well fitted by power laws, and Table 6 lists the results of the power law fitting for the SNR candidates in each galaxy. In Figure 19(a), most of the M31 SNR candidates have sizes that fall within the range of $D = 17\text{--}50$ pc. The slope of the cumulative size distribution is $\alpha = 2.53 \pm 0.04$ for $17 \text{ pc} < D < 50 \text{ pc}$. This indicates that most of the M31 SNR candidates identified in this study appear to be in the Sedov–Taylor phase. On the other hand, 6 small SNR candidates with $D < 17$ pc may still be in the free expansion phase. Figure 19(b) plots the cumulative size distribution of the M33 SNR candidates. The slope of the cumulative

size distribution we derived from the data of Gordon et al. (1998) for 47 SNR candidates is $\alpha = 2.72 \pm 0.14$ ($13 \text{ pc} < D < 33 \text{ pc}$), indicating that most of the M33 SNR candidates also appear to be in the Sedov–Taylor phase. The slopes of the cumulative size distributions of the SNR candidates in M31 and M33 are very similar, with a value of $\alpha \sim 2.5$. However, the mean size of the SNR candidates at a slope of $\alpha \sim 2.5$ ($17 < D < 50 \text{ pc}$) for M31, 36 pc, is larger than that for M33 ($13 < D < 33 \text{ pc}$), 24 pc. This shows that more large SNR candidates were found in M31 than in M33, which suggests two possibilities. First, the incompleteness of large SNR detection in our study is lower than that for M33. Second, most of the M31 SNR candidates may lie in a less dense ambient ISM than the M33 SNR candidates. On the other hand, the cumulative size distribution derived from the data of Long et al. (2010) yield $\alpha = 2.82 \pm 0.20$ for $10 \text{ pc} < D < 20 \text{ pc}$ and $\alpha = 1.60 \pm 0.03$ for $20 \text{ pc} < D < 50 \text{ pc}$. The flatter slope for large SNR candidates ($20 \text{ pc} < D < 50 \text{ pc}$) may be due to incorrect estimation of the sizes of SNR candidates, incompleteness of the SNR search, or the selection of spurious SNRs such as H II regions and superbubbles.

Figure 19(c) shows the cumulative size distribution of SNR candidates in the MCs. The slope for the size distribution of the LMC SNR candidates derived from the data of Badenes et al. (2010) is $\alpha = 1.34 \pm 0.04$ for $15 \text{ pc} < D < 55 \text{ pc}$, and that for the SMC SNR candidates is $\alpha = 1.18 \pm 0.03$ for $25 \text{ pc} < D < 50 \text{ pc}$. These results obtained from observational data indicate that most of the MC SNR candidates appear to be in the free expansion phase. However, Badenes et al. (2010) proposed that the cumulative size distribution of the MC SNR candidates is a result of the transition from the Sedov–Taylor phase to the radiative phase, which depends on the density of the ambient ISM. This explanation was supported by observations of three tracers of the density: the neutral hydrogen column density, H α surface brightness, and star formation rate based on resolved stellar populations. Figure 19(d) displays the cumulative size distribution of the MW SNR candidates. Pavlović et al. (2013) presented the sizes derived from the radio $\Sigma - D$ relation for the 274 MW SNR candidates (Green 2009). Most of them have sizes of $D = 15 - 30 \text{ pc}$, and their cumulative size distribution follows a power law. The slope for the cumulative size distribution is $\alpha = 3.60 \pm 0.06$ for $15 \text{ pc} < D < 30 \text{ pc}$. This indicates that most of the MW SNR candidates appear to be in the radiative phase, and that they might evolve more rapidly than the M31 and M33 SNR candidates.

4.4. Comparison with X-Ray Observations of M31 SNR Candidates

A comparison of the optical SNRs and X-ray SNRs in M31 is useful for determining the nature of the X-ray sources in M31 and for better characterization of the detected SNRs

and their surroundings. An interesting question is whether the optical properties of SNRs correlate with their X-ray properties. Pannuti et al. (2007) found no correlation between the X-ray and $H\alpha$ luminosities of 9 SNR candidates in M101 and NGC 2403. They suggested from the result that the interstellar media surrounding the SNR candidates are inhomogeneous rather than uniform. Leonidaki et al. (2013) also found no correlation between the X-ray and $H\alpha$ luminosities of 16 SNR candidates in five nearby galaxies. They explained that their result is due to the existence of SNR candidates surrounded by the ISM with a wide range of temperatures.

We compared our SNR catalog obtained from optical searches with the X-ray source catalog in M31 based on *XMM – Newton* observations. Pietsch et al. (2005) detected 21 X-ray SNR candidates from *XMM – Newton* data for some fields in M31. Later, the entire disk of M31 was observed by *XMM – Newton*, and a new source catalog was published by Stiele et al. (2011). They detected 1897 sources with a limit of X-ray luminosity (L_x) of $\sim 10^{35}$ erg s $^{-1}$ in the 0.2–4.5-keV band. They presented a catalog of 56 SNR candidates. More recently, Sasaki et al. (2012) inspected the SNR candidates introduced by Stiele et al. (2011) and added new SNR candidates that were bright in soft X-rays. They presented a new catalog of 46 X-ray SNR candidates in M31. Half of them matched objects in our catalog. Among the 23 objects in Sasaki et al. (2012) not matched with our catalog, 10 are non-radiative SNRs, and 9 are very diffuse and faint SNRs at optical wavelengths. Three are located outside the regions covered by the LGS, and one is embedded in a superbubble.

Figure 20 shows L_x versus the optical properties of the 23 SNR candidates in M31 common to this study and Sasaki et al. (2012). A higher fraction of SNR candidates with complete shells ($\sim 21\%$ and $\sim 80\%$ for A1-type and A2-type SNR candidates, respectively) is detected in X-rays compared to the objects of other morphological types. Figures 20(a) and (b) show a corresponding comparison of L_x to the $H\alpha$ and [S II] luminosities, respectively, of the 23 SNR candidates. L_x for the SNR candidates is nearly always less than the optical luminosity, and in many cases much less. However, there is a good correlation between the optical luminosity and L_x for the combined sample of A1-type and A2-type SNR candidates. We derived the correlation coefficients between the optical ($H\alpha$ and [S II]) luminosities and L_x for the sample, and the values are 0.52 and 0.41, respectively. Considering the number of samples, these values indicate probabilities of $\sim 98\%$ and $\sim 91\%$, respectively, that the two sets of quantities are correlated. Thus, the more luminous X-ray SNR candidates tend to have higher optical luminosity. This indicates that the ambient medium around the SNR candidates may be locally uniform.

The $H\alpha$ and [S II] surface brightnesses are compared with L_x for the 23 matched SNR candidates in Figures 20(c) and (d), respectively. The $H\alpha$ and [S II] surface brightnesses

of the A2-type SNR candidates show linear correlations with L_x . We calculated correlation coefficients of 0.62 and 0.43 for the correlations between the $H\alpha$ and $[S\ II]$ surface brightness, respectively, and L_x . Considering the number of A2-type SNR candidates, the two samples are correlated with probabilities of $\sim 97\%$ and $\sim 84\%$, respectively. The more luminous X-ray SNR candidates tend to have higher surface brightness at optical wavelengths.

Figure 20(e) shows L_x versus $[S\ II]:H\alpha$ for the SNR candidates with X-ray counterparts. L_x shows a good correlation with $[S\ II]:H\alpha$ for the combined sample of A1-type and A2-type SNR candidates. The correlation coefficient is 0.53, and it indicates a probability of $\sim 98\%$ that the two values are correlated. It is expected that stronger shocks (higher $[S\ II]:H\alpha$) would be correlated with higher L_x (Long et al. 2010; Leonidaki et al. 2013). However, we found that the SNR candidates with higher $[S\ II]:H\alpha$ are fainter in X-rays. Figure 20(f) shows L_x versus size for the 23 matched SNR candidates in M31. Although the largest SNR candidate has $D \sim 60$ pc, most of the candidates with X-ray counterparts are small ($20\text{ pc} < D < 45\text{ pc}$).

Figure 21 displays the distributions of (a) the $H\alpha$ and (b) the $[S\ II]$ surface brightness for SNR candidates with X-ray counterparts, those without such counterparts, and all SNR candidates. Most of the SNR candidates with high $H\alpha$ and $[S\ II]$ surface brightnesses have X-ray counterparts. Figures 22(a) and (b) display the differential and cumulative size distributions, respectively, of SNR candidates with X-ray counterparts, those without such counterparts, and all SNR candidates. In Figure 22(a), the SNR candidates with X-ray counterparts have a nearly flat distribution for $D = 20 - 50$ pc. The median size is 36 pc for the SNR candidates with X-ray counterparts, which is smaller than the value of 49 pc for those without such counterparts. This result is consistent with that of Long et al. (2010), who showed that the X-ray detection probability for SNR candidates with $D > 50$ pc is lower than that for candidates with $D < 50$ pc. In Figure 22(b), the slopes for the SNR candidates with X-ray counterparts and without such counterparts are similar to that for all SNR candidates, $\alpha = 2.23 \pm 0.07$ for $27\text{ pc} < D < 45\text{ pc}$ and $\alpha = 2.37 \pm 0.03$ for $25\text{ pc} < D < 55\text{ pc}$, respectively.

4.5. Spatial Distributions of Type Ia and CC SNR Candidates in M31

CC SNR candidates are typically located in the galactic plane, while Type Ia SNR candidates are found anywhere in a galaxy. For example, Franchetti et al. (2012) showed that 14 of 25 CC SNR candidates in M101 are located in the spiral arms, while 7 of 9 Type Ia SNR candidates are found in interarm regions. Figure 5 presents a similar result for the M31 SNR candidates. Most of the CC SNR candidates are concentrated in the spiral arms,

while the Type Ia SNR candidates are rather spread over the entire galaxy.

SN explosions are dominant sources of heavy elements, and they govern the evolution of the chemical abundances in galaxies. The two types of SNR candidates inject different heavy elements into the ISM of a galaxy, and therefore have a different impact on galactic chemical evolution. Type Ia explosions inject Fe-rich ejecta, while CC explosions eject O-group elements. Therefore, it is useful to estimate the relative frequency of Type Ia and CC SNR candidates.

There are a few results for the relative ratio of the two types of SNR candidates. Chu & Kennicutt (1988) examined the stellar and interstellar environments around the 32 SNR candidates in the LMC and suggested that at least 60% of them are associated with CC SNR candidates. More recently, Franchetti et al. (2012) inspected the interstellar environment and underlying stellar population of 55 SNR candidates in M101. They showed that 34 of the 55 objects are bona-fide SNRs, and $\sim 25\%$ (9 of 34) are likely Type Ia SNR candidates. We also examined the stellar and interstellar environments surrounding the 156 SNR candidates in M31, following Chu & Kennicutt (1988) and Franchetti et al. (2012). We derived a fraction of Type Ia SNR candidates, $\sim 27\%$ (42 of 156), similar to that of the M101 SNR candidates. Jennings et al. (2012) inspected the recent star formation history of the regions surrounding 59 SNR candidates in M31 using *HST* photometry. They considered that 14 of the 59 objects are Type Ia SNR candidates. We compared the positions of the 156 SNR candidates in this study with those of the 59 SNR candidates in Jennings et al. (2012). Only 31 SNR candidates in Jennings et al. (2012) match those in our catalog. The classifications of the progenitor types in this study and Jennings et al. (2012) agree for 26 of these matched SNR candidates.

Figure 23 displays the radial distributions of all, Type Ia, and CC SNR candidates detected in X-rays. The distribution of SNR candidates with X-ray counterparts shows a distinct peak at $R \sim 12$ kpc and a marginal peak at $R \sim 5$ kpc. Most of the SNR candidates at $R < 6$ kpc are Type Ia SNR candidates with X-ray counterparts. The CC SNR candidates with X-ray counterparts are located at $R \sim 12$ kpc. Figure 23 shows (b) L_x and (c) the ratio between the X-ray and $H\alpha$ luminosities of the Type Ia and CC SNR candidates with X-ray counterparts as a function of R . The X-ray luminosities for most of the Type Ia SNR candidates are brighter than those of the CC SNR candidates. The ratios between the X-ray and $H\alpha$ luminosities of the Type Ia SNR candidates are on average higher than those of the CC SNR candidates.

5. SUMMARY AND CONCLUSION

We found 76 new SNR candidates through a wide-field survey based on $H\alpha$ and $[S\ II]$ images of M31 in the LGS. In addition, we confirmed that 80 of the 234 SNR candidates in previous studies are SNR candidates according to our selection criteria. In our analysis, we investigated various properties of the 156 SNR candidates in the master catalog. The primary results are summarized as follows.

1. We attempted to classify the progenitor types of our SNR candidates according to the properties of the stellar and interstellar populations in and around each candidate. We found that 42 more likely result from Type Ia SNe, with the remainder more likely to be from CC SNe. The fraction of Type Ia SNR candidates in M31 ($\sim 23\%$) is similar to that found in M101 (Franchetti et al. 2012).
2. We classified SNR candidates considering their optical morphologies as well as their general environments. The numbers of A-type, B-type, and C-type SNR candidates are 54, 85, and 17, respectively. The numbers of shell-type and center-bright SNR candidates are 133 ($\sim 85\%$) and 23 ($\sim 15\%$), respectively. These fractions are comparable to those for the MW SNRs.
3. Most of the CC SNR candidates are concentrated in the spiral arms, while the Type Ia SNR candidates are rather spread over the entire galaxy including the inner region. The radial distribution of the CC SNR candidates shows two distinct peaks at $R \sim 12$ kpc and $R \sim 5$ kpc, while that of the Type Ia SNR candidates is broad, showing no distinct peaks. Most of the SNR candidates at $R < 7$ kpc are A-type SNR candidates, while there are more B-type SNR candidates in the outer region at $R > 7$ kpc. This indicates that the ISM at $R < 7$ kpc may be more uniform than that in other regions.
4. Most of the Type Ia SNR candidates have fainter $H\alpha$ and $[S\ II]$ luminosities than the CC SNR candidates. The $H\alpha$ luminosity function of all the SNR candidates is fitted by a double power law with a break at $L \sim 10^{36.6}$ erg s $^{-1}$. The power indices for the bright and faint parts are $\alpha = -2.61 \pm 0.42$ and $\alpha = -1.26 \pm 0.17$, respectively. The $[S\ II]$ luminosity function is fitted by a single power law with an index of $\alpha = -2.24 \pm 0.03$.
5. Most of the SNR candidates in M31 have sizes of $20\text{ pc} < D < 60\text{ pc}$. The differential size distribution of all the SNR candidates shows a strong peak at $D \sim 48$ pc with a broad wing. The differential size distribution of the CC SNR candidates shows a strong peak at $D \sim 48$ pc, while that of the Type Ia SNR candidates is much broader with a weaker peak at $D \sim 40$ pc. The differential size distribution of the A-type SNR

candidates shows a mean value of $D \sim 35$ pc, which is much smaller than that of the B-type SNR candidates, $D \sim 60$ pc.

6. The cumulative size distribution of all the SNR candidates with $17 \text{ pc} < D < 50 \text{ pc}$ is well fitted by a power law with an index of $\alpha = 2.53 \pm 0.04$. This indicates that most of the M31 SNR candidates identified in this study appear to be in the Sedov–Talyor phase. The cumulative size distribution of the CC SNR candidates with $15 \text{ pc} < D < 55 \text{ pc}$ is fitted by a power law with $\alpha = 2.30 \pm 0.04$, and that of the Type Ia SNR candidates with $25 \text{ pc} < D < 50 \text{ pc}$ is fitted by a similar power law with $\alpha = 2.45 \pm 0.06$. The difference in the size ranges between the two types of candidates indicates that most of the CC SNR candidates may lie in a denser ambient ISM than the Type Ia SNR candidates. The cumulative size distribution of the A-type SNR candidates with $25 \text{ pc} < D < 45 \text{ pc}$ is fitted by a power law with $\alpha = 2.15 \pm 0.09$, while that of the B-type SNR candidates with $35 \text{ pc} < D < 60 \text{ pc}$ is fitted by a much steeper power law with $\alpha = 4.63 \pm 0.14$. This indicates that the B-type SNR candidates may evolve faster than the A-type SNR candidates.
7. The [S II]:H α distribution of all the SNR candidates is bimodal, with peaks at [S II]:H $\alpha \sim 0.4$ and ~ 0.9 . The [S II]:H α distributions of the CC and Type Ia SNR candidates are similarly bimodal. The ratio of CC SNR candidates and Type Ia SNR candidates is higher for low [S II]:H α than for high [S II]:H α . The high [S II]:H α populations are mostly A1-type, A2-type, B1-type, and B4-type SNR candidates that have well-defined shell-like or compact shapes, while the low [S II]:H α populations are mostly A3-type, B2-type, and B3-type SNR candidates that have low surface brightness and smooth shapes. The B2-type SNR candidates are embedded in star-forming regions, and they have high H α luminosity and low [S II]:H α .
8. We inspected the radial variation in the physical properties of the SNR candidates. In the inner region ($R < 10$ kpc), the mean size of the SNRs increases from 40 pc to 60 pc as R increases, while the mean values of their H α and [S II] surface brightnesses decrease. The [S II]:H α of all the SNR candidates shows little variation with R , which is in contrast to the result given by Galarza et al. (1999).
9. The H α and [S II] luminosities of all the SNR candidates show weak or little linear correlation with their sizes. Those of the CC SNR candidates show linear correlations with their sizes, while those of the Type Ia SNR candidates show little correlation. The H α and [S II] surface brightnesses of all the SNR candidates show linear correlations with their sizes. Those of the Type Ia SNR candidates show stronger linear correlations with their sizes than those of the CC SNR candidates. The H α and [S II] luminosities of each morphological type show tight linear correlations with their sizes. The H α and

[S II] surface brightnesses of each morphological type show little linear correlation with their sizes.

10. The cumulative size distribution of the M31 SNR candidates with $17 \text{ pc} < D < 50 \text{ pc}$ is well fitted by a power law with an index of $\alpha = 2.53 \pm 0.04$. The cumulative size distribution of the M33 SNR candidates with $13 \text{ pc} < D < 33 \text{ pc}$ identified in Gordon et al. (1998) is well fitted by a power law with an index of $\alpha = 2.72 \pm 0.14$. The result is similar to that for the M31 SNR candidates, although the mean size of the M33 SNR candidates following a Sedov–Taylor phase is smaller than that of the M31 SNR candidates. This suggests two possibilities. First, the incompleteness of large SNR detection in our study is lower than that for M33. Second, most of the M31 SNR candidates may lie in a less dense ambient ISM than the M33 SNR candidates.
11. A higher fraction of SNR candidates ($\sim 21\%$ and $\sim 80\%$ for A1-type and A2-type, respectively) with relatively high surface brightnesses, small sizes, and complete shapes are detected in X-rays. We inspected the correlations between the optical properties and X-ray luminosities of the 23 SNR candidates in M31 common to this study and Sasaki et al. (2012). We found a good correlation between the optical and X-ray luminosities for the combined sample of A1-type and A2-type SNR candidates, and a better correlation between the optical surface brightness and X-ray luminosity for the A2-type SNR candidates. These results indicate that the ambient medium of the SNR candidates with X-ray counterparts has a locally uniform density.
12. The radial distribution of the SNR candidates with X-ray counterparts shows a distinct peak near 12 kpc and a broad peak near 5 kpc. Most of the SNR candidates at $R < 6 \text{ kpc}$ are Type Ia SNR candidates with X-ray counterparts. The X-ray luminosities of most of the Type Ia SNR candidates are brighter than those of the CC SNR candidates.

The authors thank Prof. Bon-Chul Koo for a fruitful discussion on SNRs and an anonymous referee for useful comments that helped improve the original manuscript significantly. This work was supported by a National Research Foundation of Korea (NRF) grant funded by the Korea Government (MSIP) (No. 2012R1A4A1028713).

REFERENCES

- Badenes, C., Harris, J., Zaritsky, D., & Prieto, J. L. 2009, *ApJ*, 700, 727
- Badenes, C., Maoz, D., & Draine, B. T. 2010, *MNRAS*, 407, 1301

- Bandiera, R., & Petruk, O. 2010, *A&A*, 509, A34
- Blair, W. P., Kirshner, R. P., & Chevalier, R. A. 1981, *ApJ*, 247, 879
- Blair, W. P., & Long, K. S. 1997, *ApJS*, 108, 261
- Blair, W. P., & Long, K. S. 2004, *ApJS*, 155, 101
- Blair, W. P., Winkler, P. F., & Long, K. S. 2012, *ApJS*, 203, 8
- Blondin, J. M., Wright, E. B., Borkowski, K. J., & Reynolds, S. P. 1998, *ApJ*, 500, 342
- Braun, R., & Walterbos, R. A. M. 1993, *A&AS*, 98, 327
- Chu, Y.-H., & Kennicutt, R. C., Jr. 1988, *AJ*, 96, 1874
- de Vaucouleurs, G. 1958, *ApJ*, 128, 465
- Dodorico, S., Benvenuti, P., & Sabbadin, F. 1978, *A&A*, 63, 63
- Dodorico, S., Dopita, M. A., & Benvenuti, P. 1980, *A&AS*, 40, 67
- Dopita, M. A., Binette, L., Dodorico, S., & Benvenuti, P. 1984, *ApJ*, 276, 653
- Dopita, M. A., Blair, W. P., Long, K. S., et al. 2010, *ApJ*, 710, 964
- Dopita, M. A., & Sutherland, R. S. 2003, *Astrophysics of the Diffuse Universe* (Berlin: Springer)
- Draine, B. T. 2011, *Physics of the Interstellar and Intergalactic Medium* (Princeton, NJ: Princeton Univ. Press), chap. 39
- Filipović, M. D., Haynes, R. F., White, G. L., & Jones, P. A. 1998, *A&AS*, 130, 421
- Filipović, M. D., Payne, J. L., Reid, W., et al. 2005, *MNRAS*, 364, 217
- Franchetti, N. A., Gruendl, R. A., Chu, Y.-H., et al. 2012, *AJ*, 143, 85
- Gaetz, T. J., Blair, W. P., Hughes, J. P., et al. 2007, *ApJ*, 663, 234
- Galarza, V. C., Walterbos, R. A. M., & Braun, R. 1999, *AJ*, 118, 2775
- Ghavamian, P., Blair, W. P., Long, K. S., et al. 2005, *AJ*, 130, 539
- Gordon, K. D., Bailin, J., Engelbracht, C. W., et al. 2006, *ApJ*, 638, L87
- Gordon, S. M., Kirshner, R. P., Long, K. S., et al. 1998, *ApJS*, 117, 89

- Green, D. A. 1984, MNRAS, 209, 449
- Green, D. A. 2009, Bull. Astron. Soc. India, 37, 45
- Hughes, J. P., & Helfand, D. J. 1984, BAAS, 16, 927
- Jennings, Z. G., Williams, B. F., Murphy, J. W., et al. 2012, ApJ, 761, 26
- Leonidaki, I., Boumis, P., & Zezas, A. 2013, MNRAS, 429, 189
- Levenson, N. A., Kirshner, R. P., Blair, W. P., & Winkler, P. F. 1995, AJ, 110, 739
- Long, K. S., Blair, W. P., Kirshner, R. P., & Winkler, P. F. 1990, ApJS, 72, 61
- Long, K. S., Blair, W. P., Winkler, P. F., et al. 2010, ApJS, 187, 495
- Long, K. S., Charles, P. A., Blair, W. P., & Gordon, S. M. 1996, ApJ, 466, 750
- Magnier, E. A., Prins, S., van Paradijs, J., et al. 1995, A&AS, 114, 215
- Massey, P., Olsen, K. A. G., Hodge, P. W., et al. 2006, AJ, 131, 2478
- Mathewson, D. S., Ford, V. L., Dopita, M. A., et al. 1983, ApJS, 51, 345
- Mathewson, D. S., & Healey, J. R. 1964, in IAU Symp. 20, The Galaxy and the Magellanic Clouds, ed. Kerr, F. J. & Rodgers, A. W. (Canberra: Australian Acad. of Sciences), 245
- Matonick, D. M., & Fesen, R. A. 1997, ApJS, 112, 49
- Matonick, D. M., Fesen, R. A., Blair, W. P., & Long, K. S. 1997, ApJS, 113, 333
- McKee, C. F., & Ostriker, J. P. 1977, ApJ, 218, 148
- Mills, B. Y., Turtle, A. J., Little, A. G., & Durdin, J. M. 1984, Aust. J. Phys., 37, 321
- Misanovic, Z., Pietsch, W., Haberl, F., et al. 2006, A&A, 448, 1247
- Pannuti, T. G., Duric, N., Lacey, C. K., et al. 2002, ApJ, 565, 966
- Pannuti, T. G., Schlegel, E. M., & Lacey, C. K. 2007, AJ, 133, 1361
- Pavlović, M. Z., Urošević, D., Vukotić, B., Arbutina, B., & Göker, Ü. D. 2013, ApJS, 204, 4
- Payne, J. L., White, G. L., & Filipović, M. D. 2008, MNRAS, 383, 1175
- Pietsch, W., Freyberg, M., & Haberl, F. 2005, A&A, 434, 483

- Pietsch, W., Misanovic, Z., Haberl, F., et al. 2004, *A&A*, 426, 11
- Plucinsky, P. P., Williams, B., Long, K. S., et al. 2008, *ApJS*, 174, 366
- Raymond, J. C. 1979, *ApJS*, 39, 1
- Riess, A. G., Fliri, J., & Valls-Gabaud, D. 2012, *ApJ*, 745, 156
- Sasaki, M., Pietsch, W., Haberl, F., et al. 2012, *A&A*, 544, A144
- Smith, C., Leiton, R., & Pizarro, S. 2000, *ASP Conf. Ser. Vol. 221, Stars, Gas and Dust in Galaxies: Exploring the Links*, ed. Alloin, D., Olsen, K., & Galaz, G. (San Francisco: Astron. Soc. Pac.), 83
- Smith, R. C., Kirshner, R. P., Blair, W. P., & Winkler, P. F. 1991, *ApJ*, 375, 652
- Sonbas, E., Akyuz, A., & Balman, S. 2009, *A&A*, 493, 1061
- Stiele, H., Pietsch, W., Haberl, F., et al. 2011, *A&A*, 534, A55
- Truelove, J. K., & McKee, C. F. 1999, *ApJS*, 120, 299
- van der Heyden, K. J., Bleeker, J. A. M., & Kaastra, J. S. 2004, *A&A*, 421, 1031
- Vilardell, F., Ribas, I., Jordi, C., Fitzpatrick, E. L., & Guinan, E. F. 2010, *A&A*, 509, A70
- Williams, R. M., Chu, Y.-H., Dickel, J. R., et al. 1999, *ApJS*, 123, 467
- Woltjer, L. 1972, *ARA&A*, 10, 129

Table 1. A Catalog of Previous M31 SNR Candidates Rejected in This Study

Name ^a	R.A. (J2000.0) ^b [Degree]	Dec. (J2000.0) ^b [Degree]	$\log L(\text{H}\alpha)^c$ [erg s ⁻¹]	$\log L([\text{S II}])^c$ [erg s ⁻¹]	D^d [pc]	[S II]:H α	Class. ^e
M95-1-3	10.2798777	41.071918	36.96	36.60	86.2	0.43	HO
M95-1-4	10.3583202	41.201523	37.00	36.62	60.6	0.42	HO
M95-1-5	10.4346228	40.755898	37.29	36.77	150.2	0.30	S
M95-1-11	10.9159412	41.818584	36.68	36.22	83.0	0.35	H
M95-1-12	11.0364685	41.527878	36.87	36.24	64.0	0.23	H
M95-2-1	10.0010300	40.346230	36.07	35.58	40.2	0.32	H
M95-2-2	10.0218763	40.503647	36.58	36.45	131.4	0.75	S
M95-2-6	10.1666679	40.789879	35.96	36.16	90.4	1.58	D
M95-2-5	10.1676588	40.706387	36.32	35.58	41.8	0.18	H

^aD80: Dodorico et al. (1980); BA: Blair et al. (1981); K: Braun & Walterbos (1993); M95: Magnier et al. (1995).

^bMeasured in the H α image.

^cCalculated using $L = 4\pi d^2 \times \text{flux}$ for $d = 750$ kpc.

^dDiameter calculated using $1'' = 3.63$ pc.

^eH: H II regions with [S II]:H $\alpha < 0.4$; HO: H II regions with $0.4 < [\text{S II}]:\text{H}\alpha < 0.6$ and blue stars inside; S: Superbubbles (Larger than $D = 100$ pc and a number of blue stars inside); D: Diffuse ionized gas ([S II]:H $\alpha > 0.8$, but very low surface brightnesses).

(This table is available in its entirety in machine-readable form in the online journal. A portion is shown here for guidance regarding its form and content.)

Table 2. Characteristics of M31 SNR Candidates of Different Morphological Types

Type	Number ^a	$L(\text{H}\alpha)$	$L([\text{SII}])$	D	$[\text{SII}]:\text{H}\alpha$	Environment	Description
A1	28(6)	moderate	moderate	small	high	isolated	complete shells
A2	15(6)	high	high	small	high	isolated	compact and center-bright remnants
A3	11(4)	moderate	low	small	low	isolated	diffuse and extended shells
B1	20(4)	low	moderate	large	high	isolated	partial shells
B2	28(4)	high	high	large	low	confused	bright partial shells
B3	24(8)	moderate	moderate	large	low	isolated	diffuse partial shells
B4	13(7)	low	moderate	large	high	isolated	shells with brightening on one side
C ^b	17(3)	—	—	—	—	—	—

^aValues in parentheses represent numbers of Type Ia SNR candidates.

^bAmbiguous objects, excluding A-type and B-type SNR candidates.

Table 3. A Catalog of M31 SNR Candidates

ID	R.A. (J2000.0) ^a [Degree]	Dec. (J2000.0) ^a [Degree]	$\log L(\text{H}\alpha)$ ^b [erg s ⁻¹]	$\log L([\text{S II}])$ ^b [erg s ⁻¹]	D ^c [pc]	[S II]:H α	Morphology type	$N(\text{OB})$ ^d	$N(\text{HII})$ ^e	Progenitor type	Comments ^f
1	9.4056797	39.862778	35.72	35.65	47.0	0.86	C	0	0	Ia	
2	9.8472862	40.738834	36.54	36.57	55.4	1.06	A	6	0	CC	BA474
3	9.8783941	40.357998	35.68	35.66	32.0	0.96	A	8	2	CC	
4	9.9373655	40.498367	36.33	36.37	45.6	1.09	A	0	1	CC	M95-1-1
5	9.9593277	40.349838	36.47	36.07	53.8	0.40	B2	3	2	CC	M95-3-8
6	9.9684820	40.495148	36.88	36.71	71.0	0.67	B2	1	0	CC	M95-1-2
7	10.0466290	40.960224	35.72	35.86	72.0	1.37	C	0	0	Ia	
8	10.0589018	40.620914	35.75	35.85	51.6	1.26	B	9	0	CC	
9	10.1020517	40.815052	35.97	35.99	41.0	1.03	A	2	0	CC	
10	10.1265640	40.721081	34.60	34.35	7.6	0.56	D	58	3	CC	

^aMeasured in the H α image.

^bCalculated using $L = 4\pi d^2 \times \text{flux}$ for $d = 750$ kpc.

^c $1'' = 3.63$ pc for $d = 750$ kpc.

^dNumber of OB stars located between the boundary of each SNR candidate and 100 pc from the center of each SNR.

^eNumber of H II regions with $L > 10^{36}$ erg s⁻¹ located between the boundary of each SNR candidate and 100 pc from the center of each SNR.

^fBA: Blair et al. (1981); K: Braun & Walterbos (1993); M95: Magnier et al. (1995).

(This table is available in its entirety in machine-readable form in the online journal.

A portion is shown here for guidance regarding its form and content.)

Table 4. Fitting Results for $L - D$ and $\Sigma - D$ Relations for SNR Candidates in M31

	Sample	N	Fitting range	Luminosity–Size ($L - D$)			Surface brightness–Size ($\Sigma - D$)		
				a (slope)	b (zero point)	rms	a (slope)	b (zero point)	rms
$H\alpha$	All	156	8 pc < D < 100 pc	2.14±0.12	32.57±0.19	0.77	—	—	—
	All ^a	139	21 pc < D < 100 pc	2.05±0.18	32.72±0.30	0.40	-1.78±0.18	12.29±0.30	0.35
	Type Ia	42	15 pc < D < 100 pc	—	—	—	-2.20±0.27	11.65±0.47	0.80
	Type Ia ^a	39	26 pc < D < 100 pc	—	—	—	-2.40±0.24	11.28±0.40	0.52
	CC	114	8 pc < D < 91 pc	2.39±0.14	32.20±0.23	1.01	—	—	—
	CC ^a	100	21 pc < D < 91 pc	2.49±0.20	32.02±0.34	0.44	—	—	—
[S II]	All	156	8 pc < D < 100 pc	2.06±0.11	32.59±0.18	0.75	—	—	—
	All ^a	139	21 pc < D < 100 pc	1.90±0.17	32.85±0.28	0.37	-1.87±0.18	12.27±0.31	0.37
	Type Ia	42	15 pc < D < 100 pc	—	—	—	-2.24±0.28	11.69±0.49	0.82
	Type Ia ^a	39	26 pc < D < 100 pc	—	—	—	-2.42±0.30	11.37±0.51	0.54
	CC	114	8 pc < D < 91 pc	2.26±0.12	32.27±0.19	0.97	—	—	—
	CC ^a	100	21 pc < D < 91 pc	2.22±0.18	32.33±0.31	0.40	—	—	—

^aExcluding C-type SNR candidates.

Table 5. Fitting Results for $L - D$ and $\Sigma - D$ Relations for M31 SNR Candidates of Different Morphological Types

	Sample	N	Fitting range	Luminosity–Size ($L - D$)			Surface brightness–Size ($\Sigma - D$)		
				a (slope)	b (zero point)	rms	a (slope)	b (zero point)	rms
H α	A1-type	28	22 pc < D < 60 pc	2.13 \pm 0.22	32.60 \pm 0.35	0.39	—	—	—
	A2-type	15	21 pc < D < 48 pc	2.18 \pm 0.30	33.20 \pm 0.46	0.35	—	—	—
	A3-type	11	21 pc < D < 49 pc	1.53 \pm 0.29	33.59 \pm 0.45	0.31	—	—	—
	B1-type	20	32 pc < D < 76 pc	2.21 \pm 0.13	32.10 \pm 0.21	0.42	—	—	—
	B2-type	28	36 pc < D < 89 pc	2.34 \pm 0.19	32.51 \pm 0.33	0.34	-1.32 \pm 0.29	12.60 \pm 0.44	0.25
	B3-type	24	42 pc < D < 91 pc	2.09 \pm 0.18	32.43 \pm 0.32	0.28	-1.19 \pm 0.15	13.40 \pm 0.23	0.24
	B4-type	13	30 pc < D < 100 pc	1.89 \pm 0.12	32.45 \pm 0.22	0.53	—	—	—
[S II]	A1-type	28	22 pc < D < 60 pc	2.30 \pm 0.28	32.32 \pm 0.45	0.43	—	—	—
	A2-type	15	21 pc < D < 48 pc	2.03 \pm 0.29	33.41 \pm 0.45	0.32	—	—	—
	A3-type	11	21 pc < D < 49 pc	1.45 \pm 0.26	33.33 \pm 0.40	0.29	—	—	—
	B1-type	20	32 pc < D < 76 pc	2.02 \pm 0.12	32.49 \pm 0.21	0.38	—	—	—
	B2-type	28	36 pc < D < 89 pc	2.44 \pm 0.31	32.05 \pm 0.53	0.35	-1.51 \pm 0.32	12.36 \pm 0.49	0.27
	B3-type	24	42 pc < D < 91 pc	2.06 \pm 0.16	32.24 \pm 0.27	0.28	-1.24 \pm 0.18	13.71 \pm 0.28	0.25
	B4-type	13	30 pc < D < 100 pc	1.88 \pm 0.15	32.47 \pm 0.27	0.53	—	—	—

Table 6. Power Law Indices for Cumulative Size Distributions of SNR Candidates in Nearby Galaxies

Galaxies	N	Fitting range of D	α^*	Phase	Reference	Wavelength
M31	85	$17 \text{ pc} < D < 50 \text{ pc}$	2.53 ± 0.04	Sedov–Taylor	This study	Optical (LGS)
M33	47	$13 \text{ pc} < D < 33 \text{ pc}$	2.72 ± 0.14	Sedov–Taylor	Gordon et al. (1998)	Optical
M33	17	$10 \text{ pc} < D < 20 \text{ pc}$	2.82 ± 0.20	–	Long et al. (2010)	X-ray, Optical (LGS)
M33	69	$20 \text{ pc} < D < 50 \text{ pc}$	1.60 ± 0.03	–	Long et al. (2010)	X-ray, Optical (LGS)
LMC	33	$15 \text{ pc} < D < 55 \text{ pc}$	1.34 ± 0.04	Free expansion	Badenes et al. (2010)	X-ray, Optical, Radio
SMC	11	$25 \text{ pc} < D < 50 \text{ pc}$	1.18 ± 0.03	Free expansion	Badenes et al. (2010)	X-ray, Optical, Radio
MW	111	$15 \text{ pc} < D < 30 \text{ pc}$	3.60 ± 0.06	Radiative	Pavlović et al. (2013)	Radio ($\Sigma - D$ relation)

*We derived the power law indices using the catalogs of SNR candidates in the references.

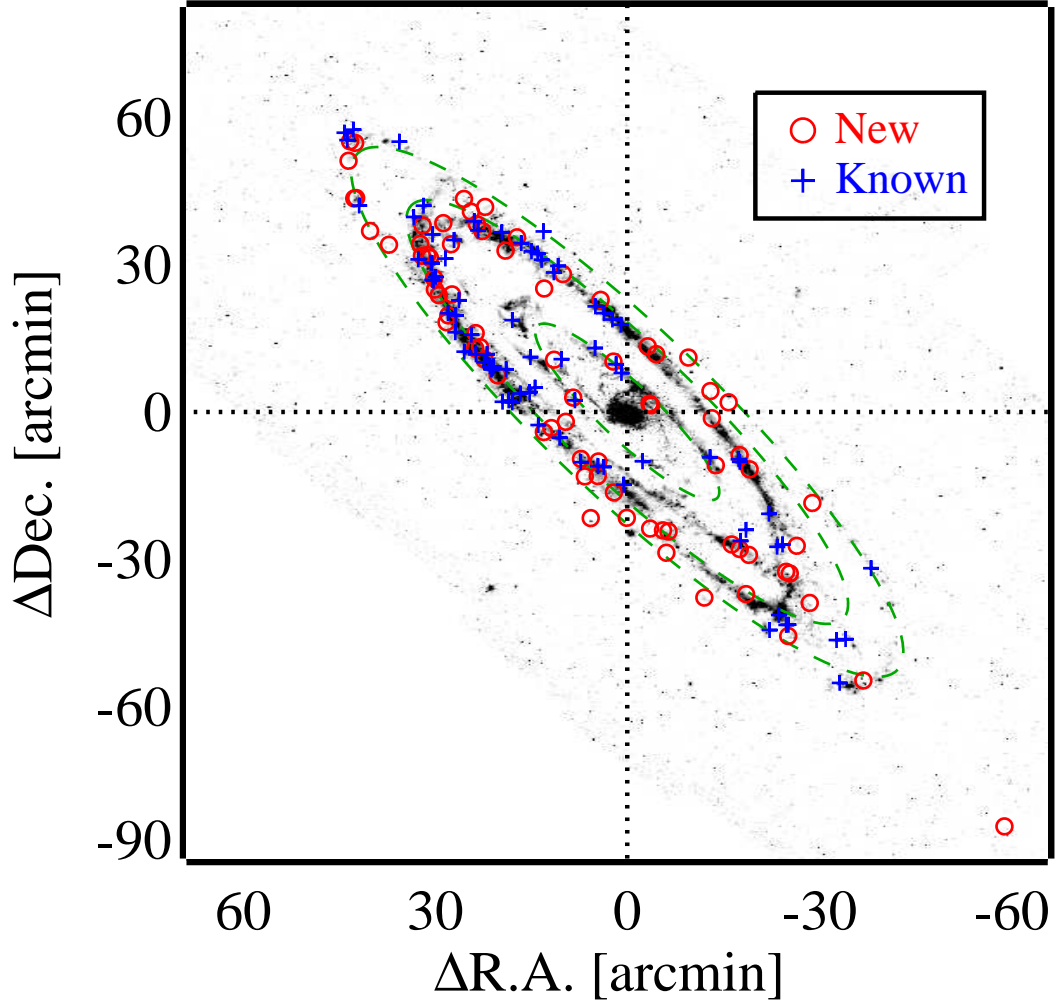


Fig. 1.— Spatial distribution of M31 SNR candidates newly found in this study (circles) in comparison with those presented in previous studies (plus signs). Background is a gray-scale map of the *Spitzer* MIPS 24 μm band image, clearly showing the star-forming regions in the spiral arms and ring structures at 5, 12, and 15 kpc (Gordon et al. 2006). Dashed ellipses mark 5, 12, and 15 kpc rings.

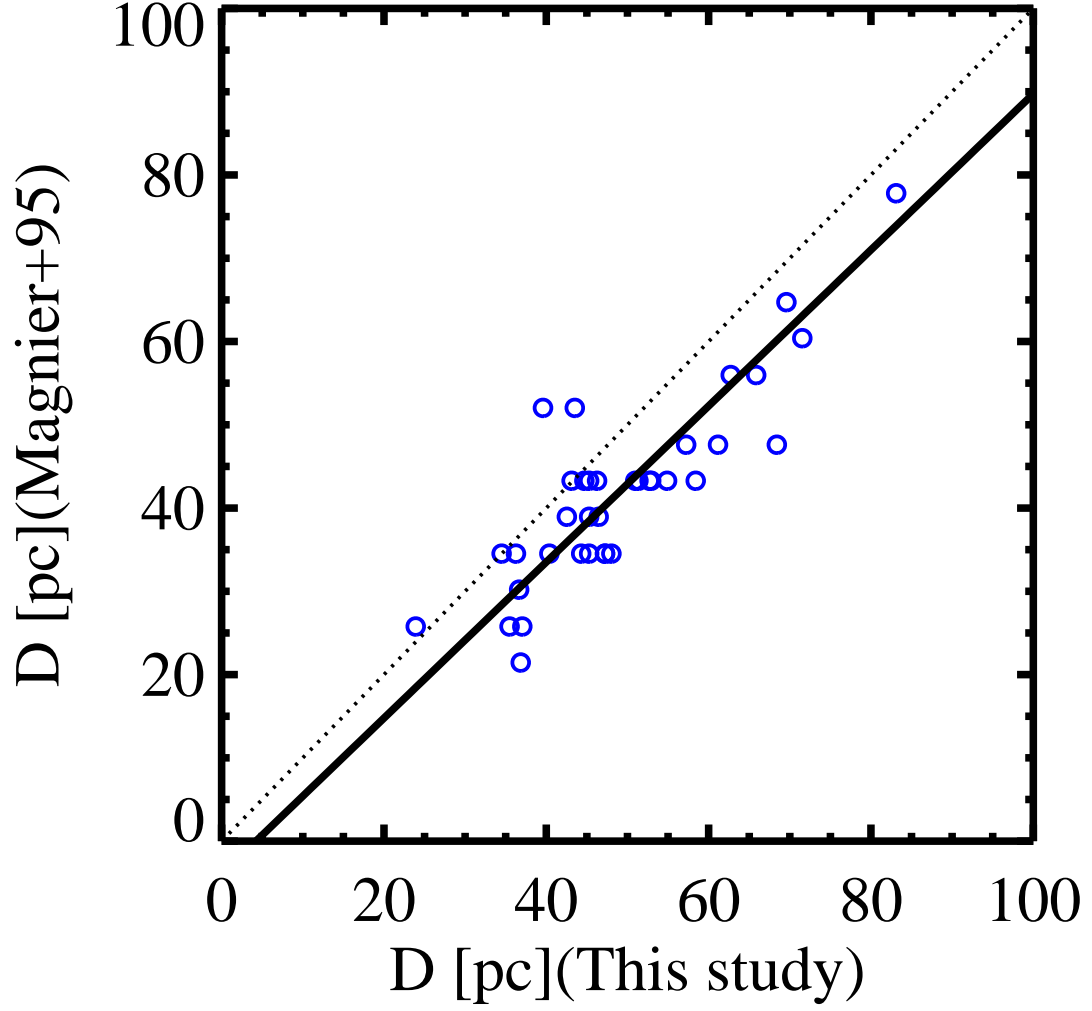


Fig. 2.— Comparison of measured sizes of M31 SNR candidates common to this study and Magnier et al. (1995). Dotted line denotes one-to-one relation, and solid line represents linear least-squares fit: D (this study) = $1.07(\pm 0.08) \times D$ (Magnier et al. 1995) + $4.2(\pm 3.4)$ pc.

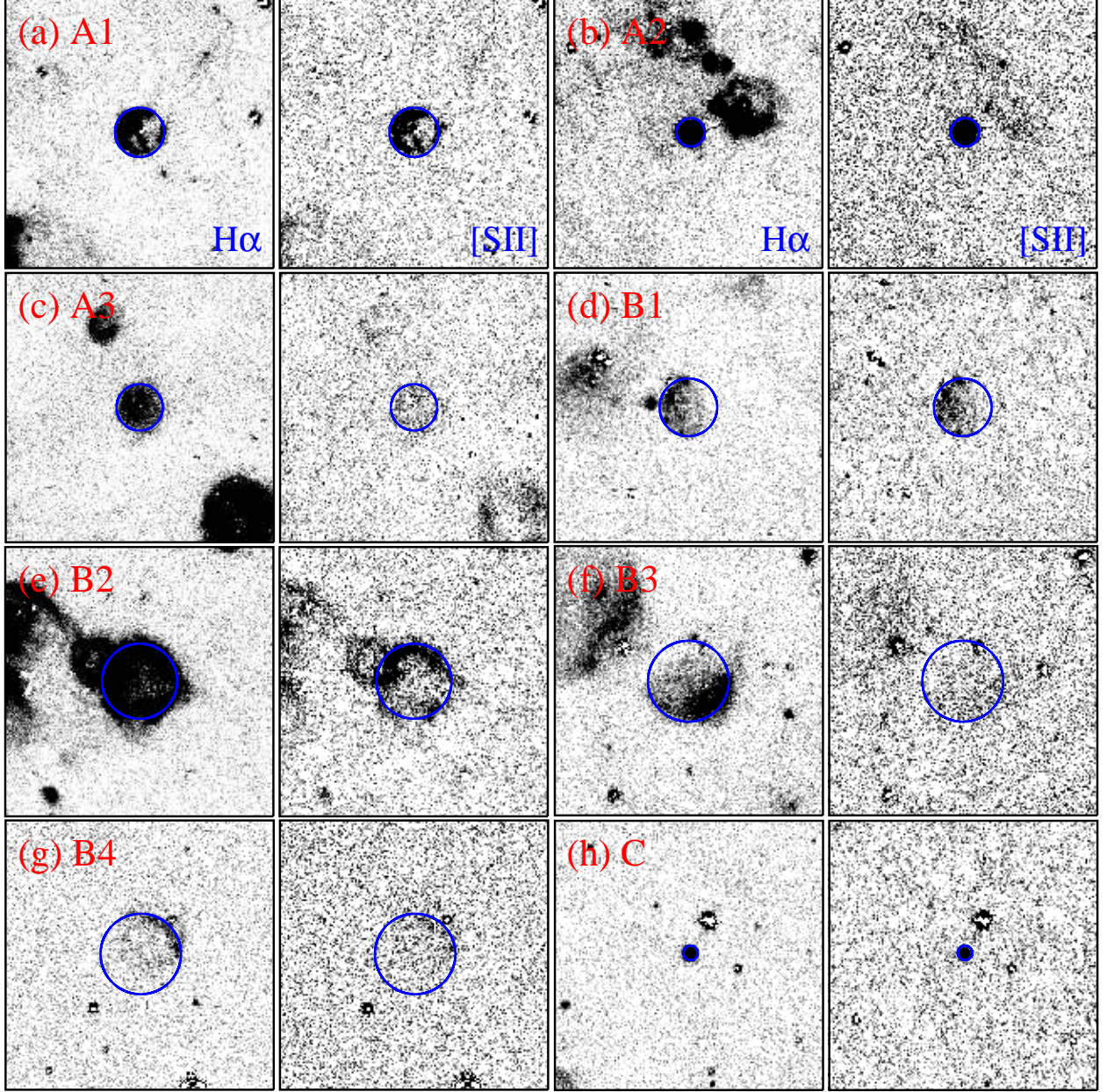


Fig. 3.— Gray-scale maps of continuum-subtracted H α and [S II] images for samples of M31 SNR candidates of different morphological types. (a) A1-type, (b) A2-type, (c) A3-type, (d) B1-type, (e) B2-type, (f) B3-type, (g) B4-type, and (h) C-type SNR candidates. Circles indicate sizes of SNR candidates. Field of view for each image is $67''.5 \times 67''.5$ ($245 \text{ pc} \times 245 \text{ pc}$). North is up, and east to the left.

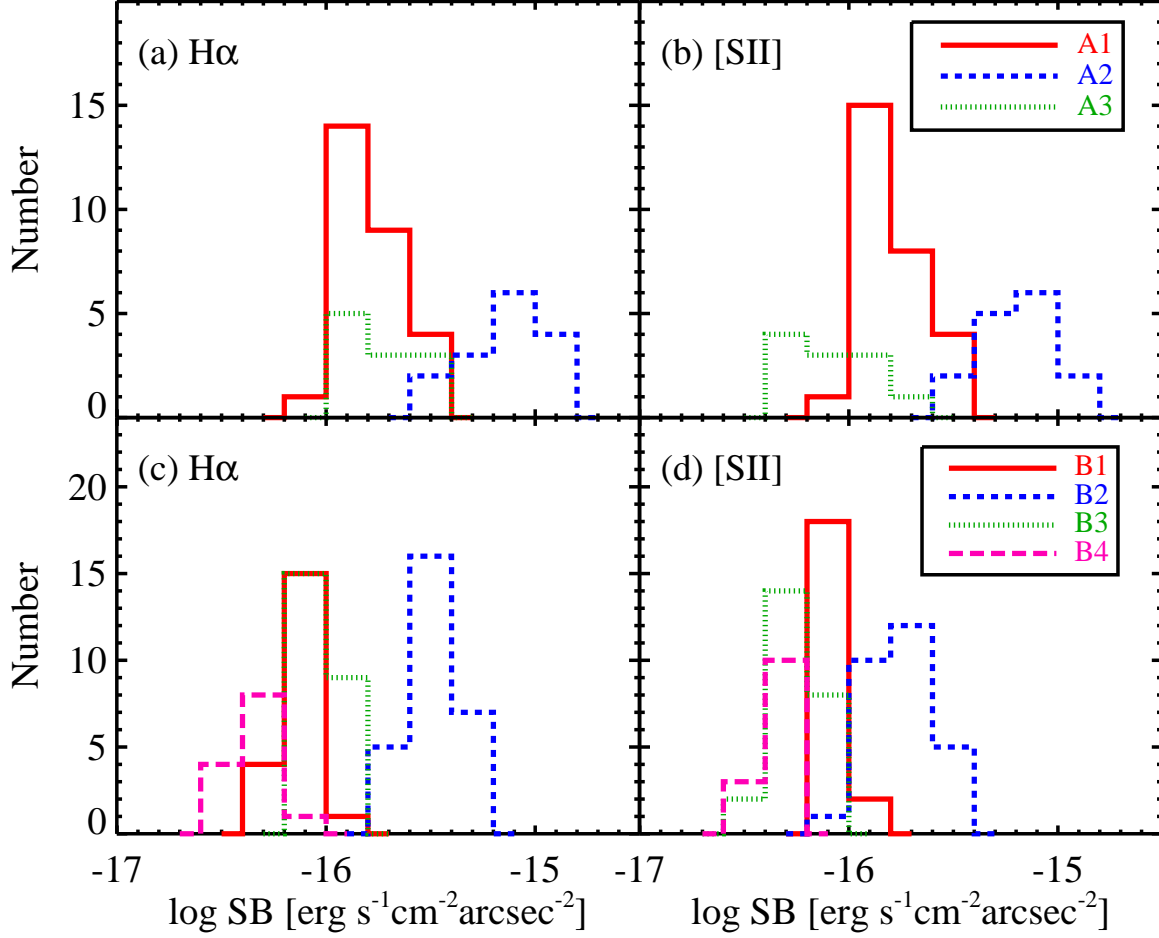


Fig. 4.— (Upper panels) Distributions of H α and [S II] surface brightnesses for A1-type (solid line), A2-type (dashed line), and A3-type (dotted line) SNR candidates in M31. (Lower panels) Same as above, but for B1-type (solid line), B2-type (dashed line), B3-type (dotted line), and B4-type (long-dashed line) SNR candidates in M31.

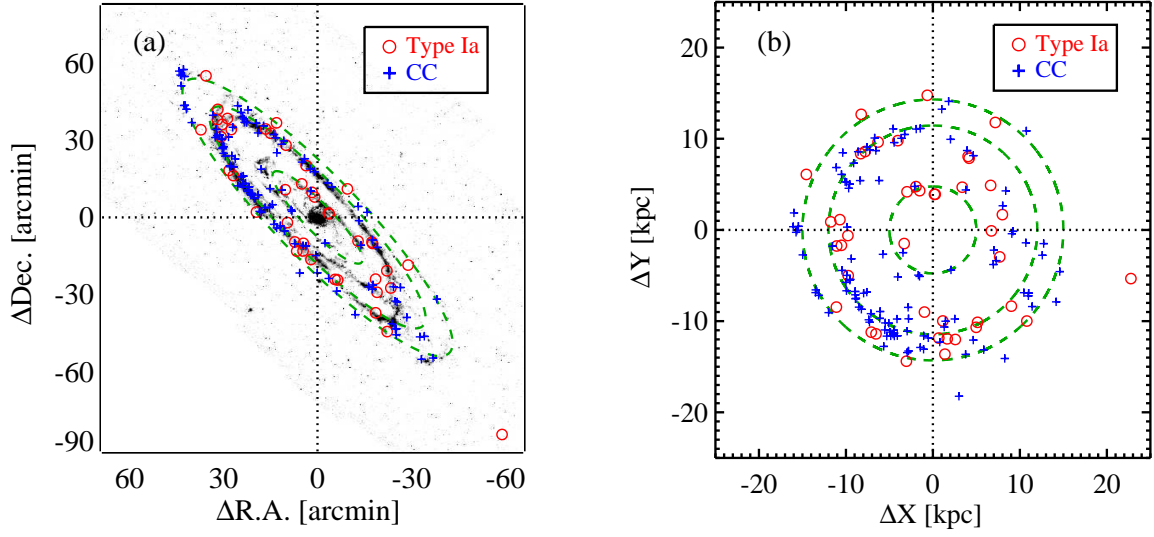


Fig. 5.— (a) Spatial distributions of Type Ia (circles) and CC (plus signs) SNR candidates in M31 on the sky. Background is a gray-scale map of the *Spitzer* MIPS 24 μm band image. Dashed ellipses mark 5, 12, and 15 kpc rings. (b) Spatial distributions of M31 SNR candidates in the plane deprojected according to the inclination angle of M31. Dashed circles mark 5 kpc, 12 kpc, and 15 kpc rings.

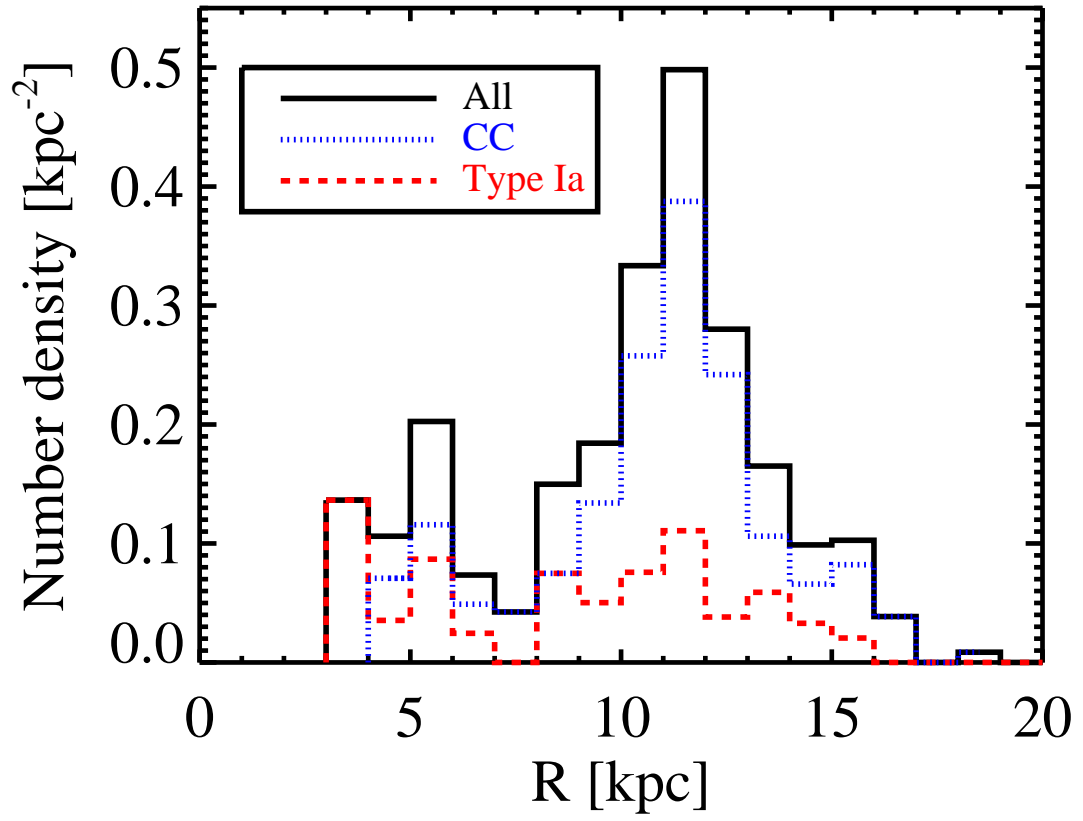


Fig. 6.— Radial distributions of number density of all (solid line), CC (dotted line), and Type Ia (dashed line) SNR candidates in M31.

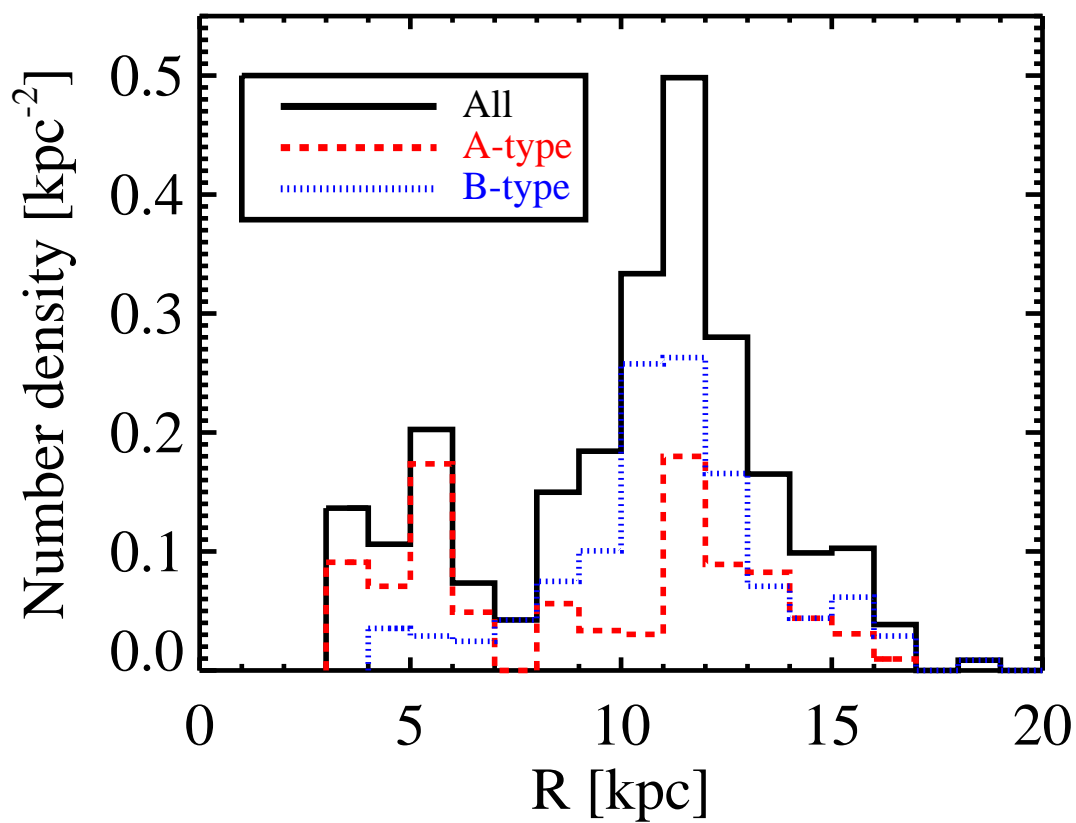


Fig. 7.— Radial distributions of number density of all (solid line), A-type (dashed line), and B-type (dotted line) SNR candidates in M31.

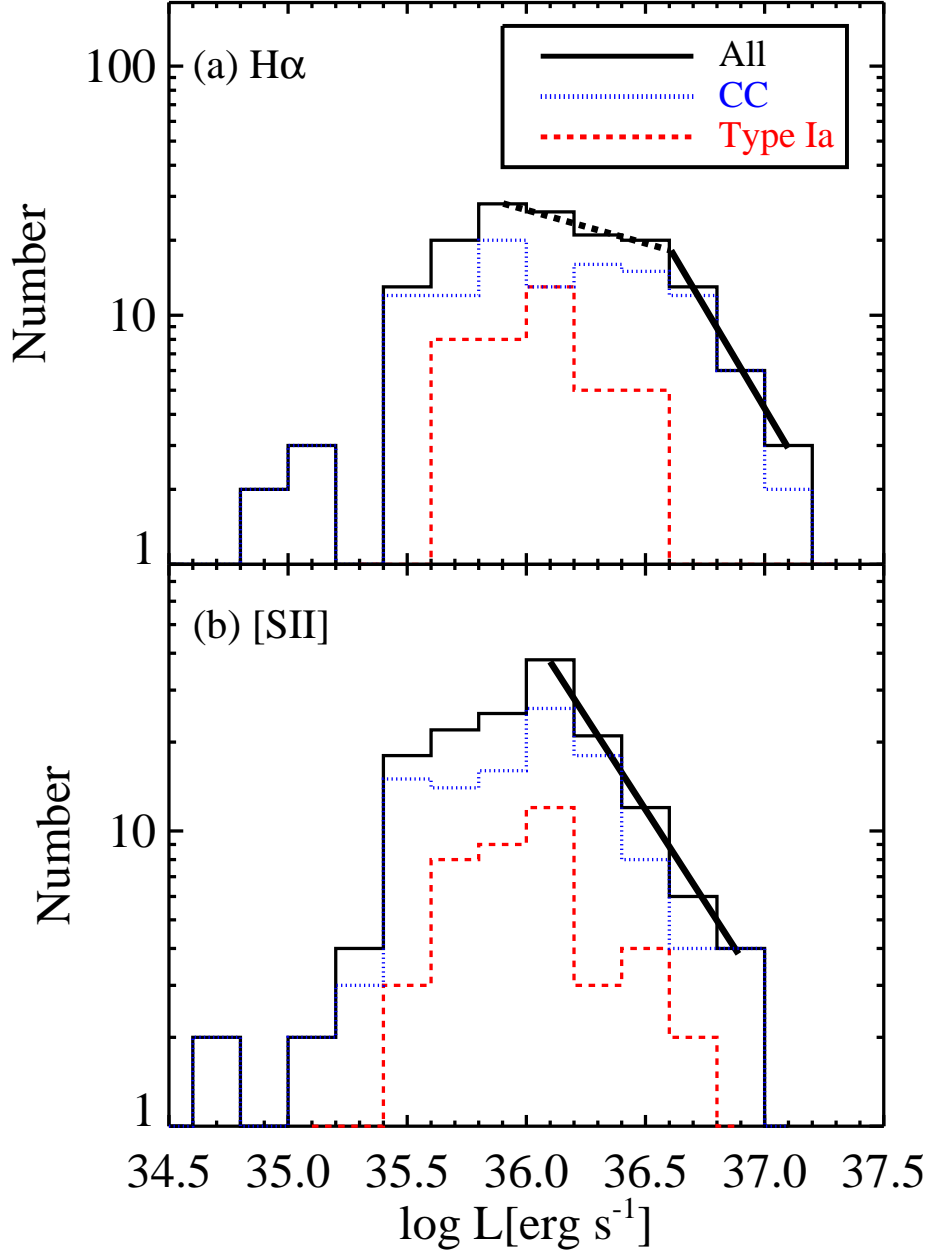


Fig. 8.— (a) H α and (b) [S II] luminosity functions of all (solid line), CC (dotted line), and Type Ia (dashed line) SNR candidates in M31. Thick dashed and thick solid lines in (a) represent a double power law fit for the faint part ($L < 10^{36.6} \text{ erg s}^{-1}$) and the bright part ($L > 10^{36.6} \text{ erg s}^{-1}$), respectively. The power law indices are $\alpha = -2.61 \pm 0.42$ for the bright part and $\alpha = -1.26 \pm 0.17$ for the faint part. Thick solid line in (b) represents a single power law fit for the bright part ($L > 10^{36} \text{ erg s}^{-1}$), with an index of $\alpha = -2.24 \pm 0.03$.

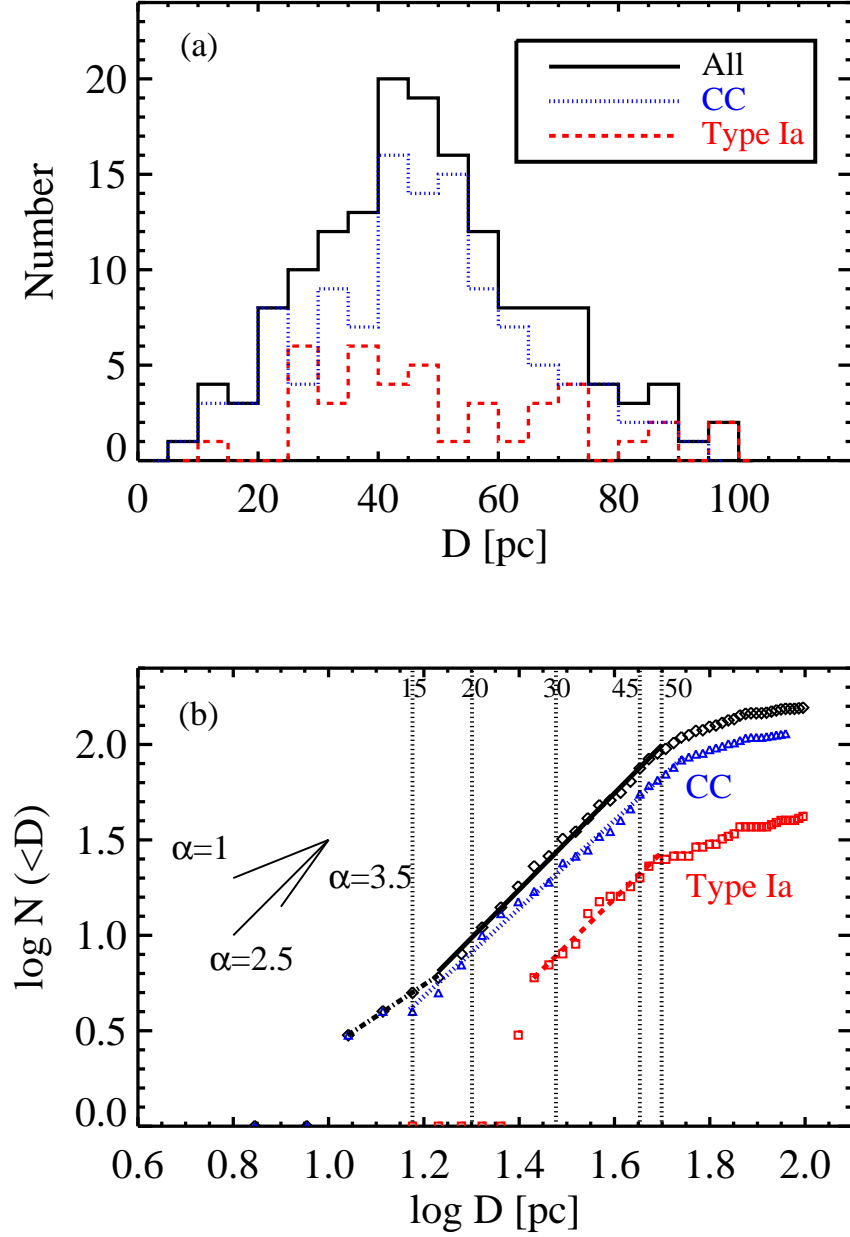


Fig. 9.— (a) Differential size distributions of all (solid line), CC (dotted line), and Type Ia (dashed line) SNR candidates in M31. (b) Cumulative size distributions of all (diamonds), CC (triangles), and Type Ia (squares) SNR candidates in M31. Thick lines represent power law fits. The power law indices for all SNR candidates are $\alpha = 1.65 \pm 0.02$ (dot-dashed line) for $D < 17$ pc and $\alpha = 2.53 \pm 0.04$ (solid line) for $17 \text{ pc} < D < 50$ pc. The power law index for CC SNR candidates is $\alpha = 2.30 \pm 0.04$ (dotted line) for $15 \text{ pc} < D < 55$ pc, while that for Type Ia SNR candidates is $\alpha = 2.45 \pm 0.06$ (dashed line) for $25 \text{ pc} < D < 50$ pc. Vertical lines represent references for linear sizes of fitting ranges.

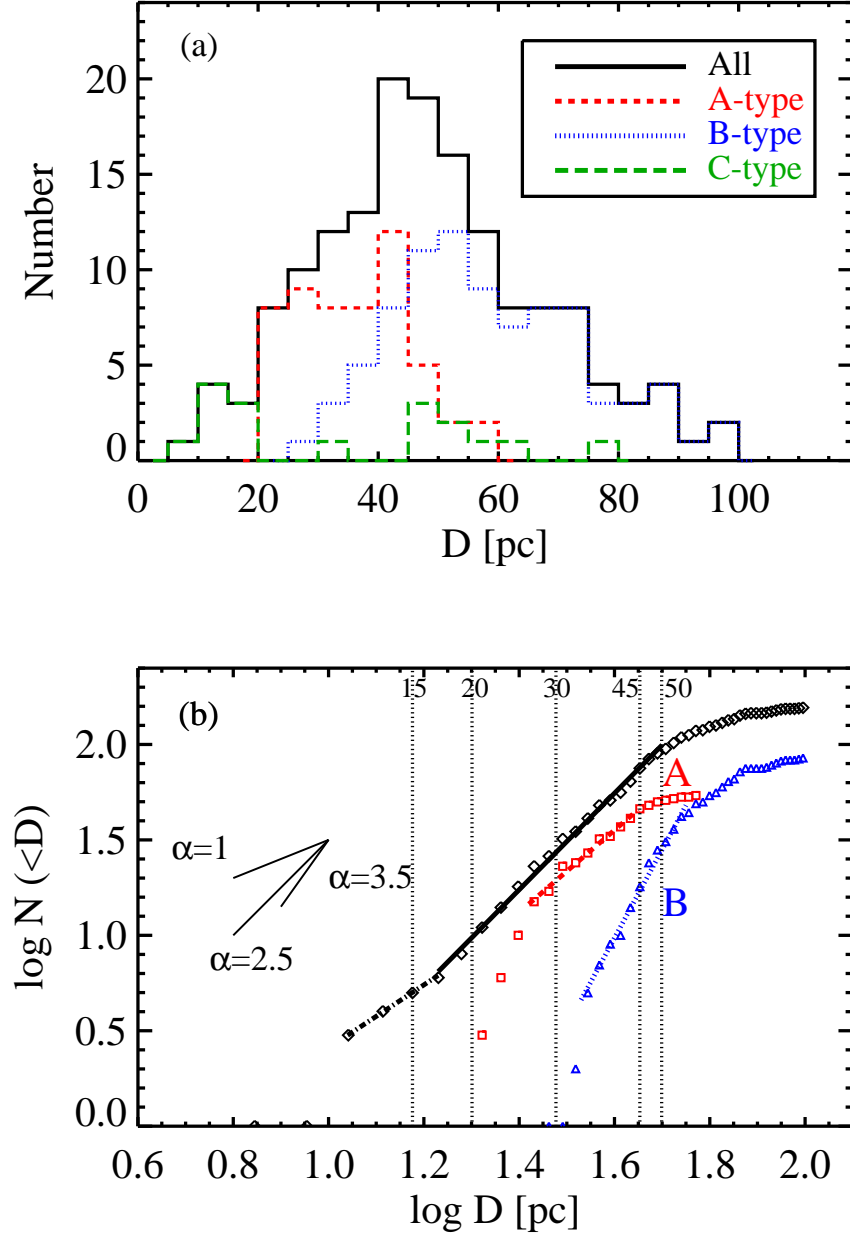


Fig. 10.— (a) Differential size distributions of all (solid line), A-type (dashed line), B-type (dotted line), and C-type (long-dashed line) SNR candidates in M31. (b) Cumulative size distributions of all (diamonds), A-type (squares), and B-type (triangles) SNR candidates in M31. Thick lines represent power law fits. The power law index for A-type SNR candidates is $\alpha = 2.15 \pm 0.09$ (dashed line) for $25 \text{ pc} < D < 45 \text{ pc}$, while that for B-type SNR candidates is $\alpha = 4.63 \pm 0.14$ (dotted line) for $35 \text{ pc} < D < 60 \text{ pc}$.

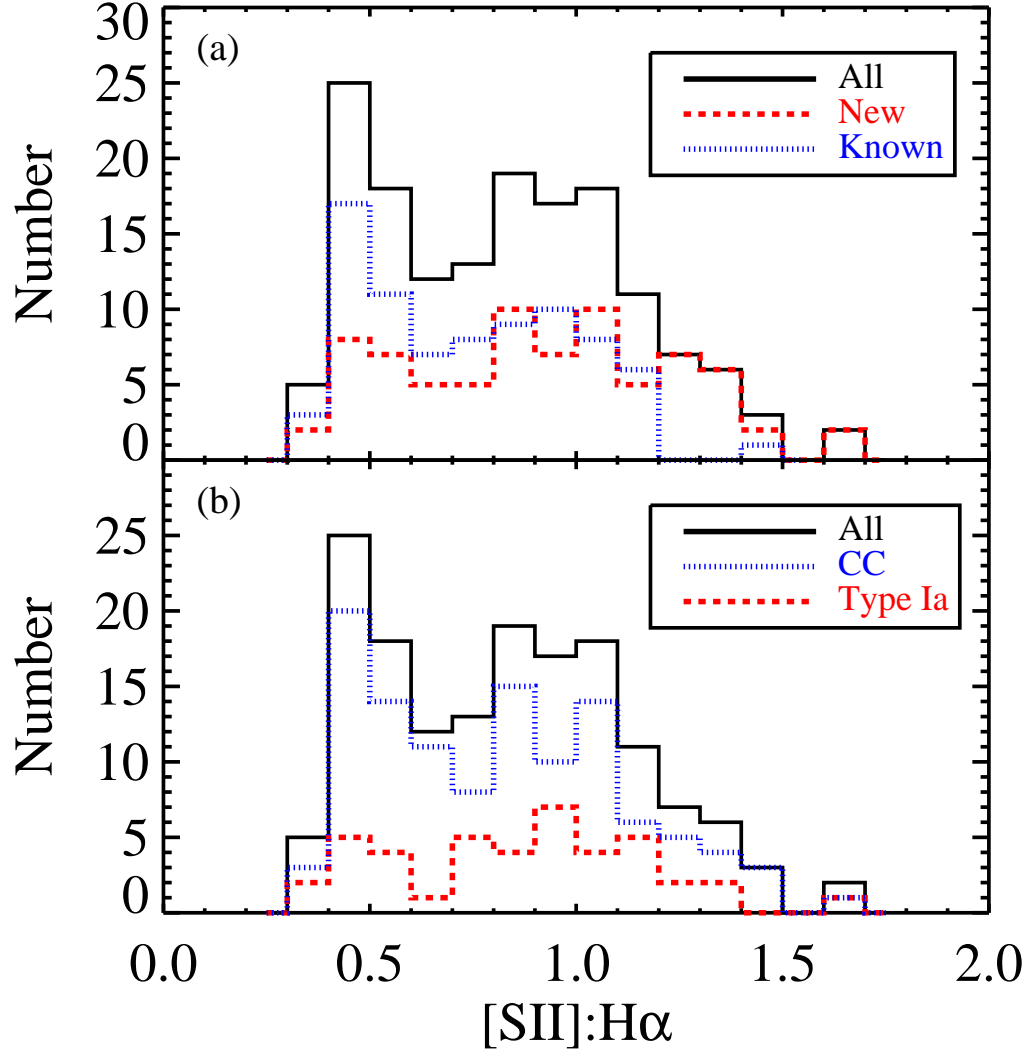


Fig. 11.— (a) $[\text{S II}]:\text{H}\alpha$ distributions of all SNR candidates (solid line), new SNR candidates (dashed line), and known SNR candidates (dotted line) in M31. (b) $[\text{S II}]:\text{H}\alpha$ distributions of all (solid line), CC (dotted line), and Type Ia (dashed line) SNR candidates in M31.

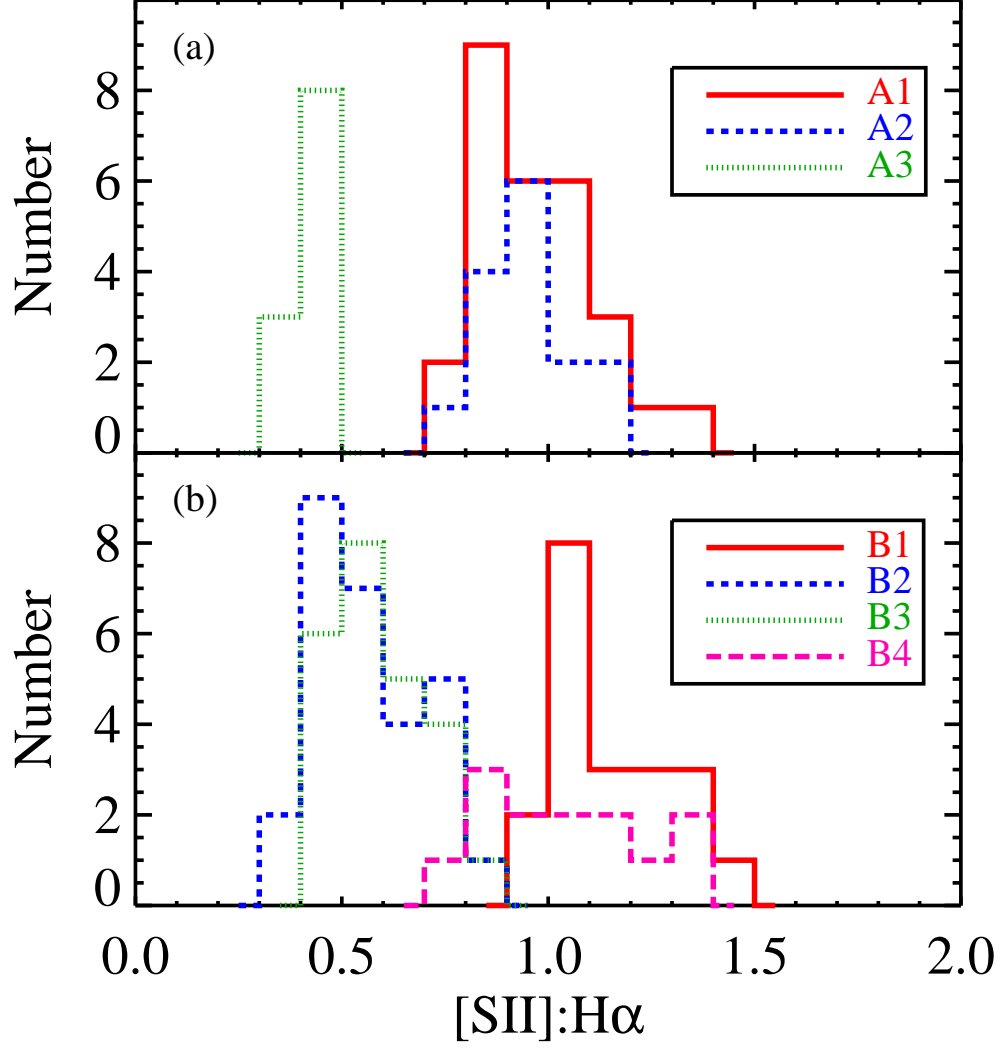


Fig. 12.— (a) [S II]:H α distributions of A1-type (solid line), A2-type (dashed line), and A3-type (dotted line) SNR candidates in M31. (b) [S II]:H α distributions of B1-type (solid line), B2-type (dashed line), B3-type (dotted line), and B4-type (long-dashed line) SNR candidates in M31.

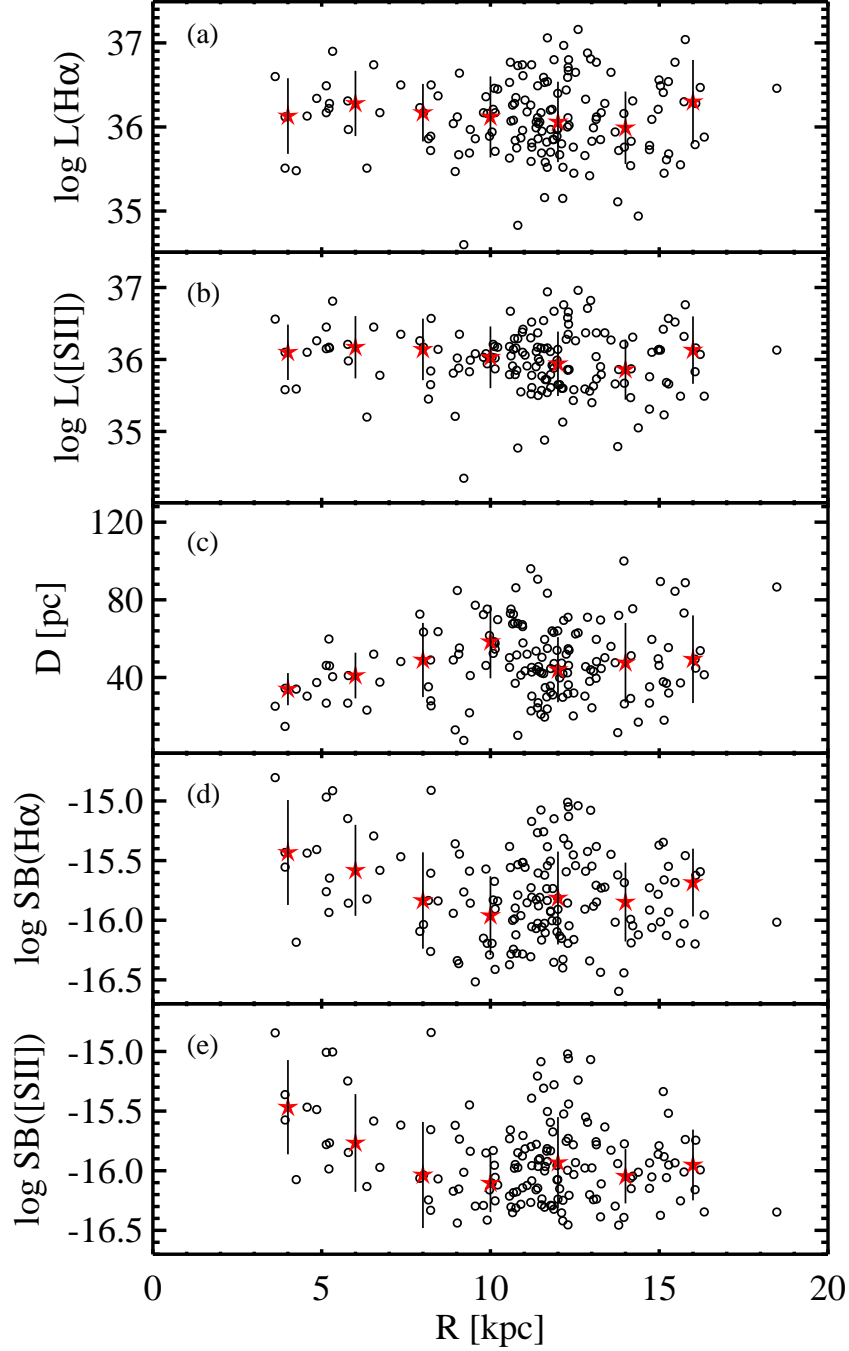


Fig. 13.— (a) $\text{H}\alpha$ luminosity, (b) $[\text{S II}]$ luminosity, (c) size, (d) $\text{H}\alpha$ surface brightness, and (e) $[\text{S II}]$ surface brightness of M31 SNR candidates as a function of deprojected galactocentric distance (R). Star symbols indicate mean values in a distance bin of 2 kpc. Vertical error bars denote standard deviations of values in distance bin.

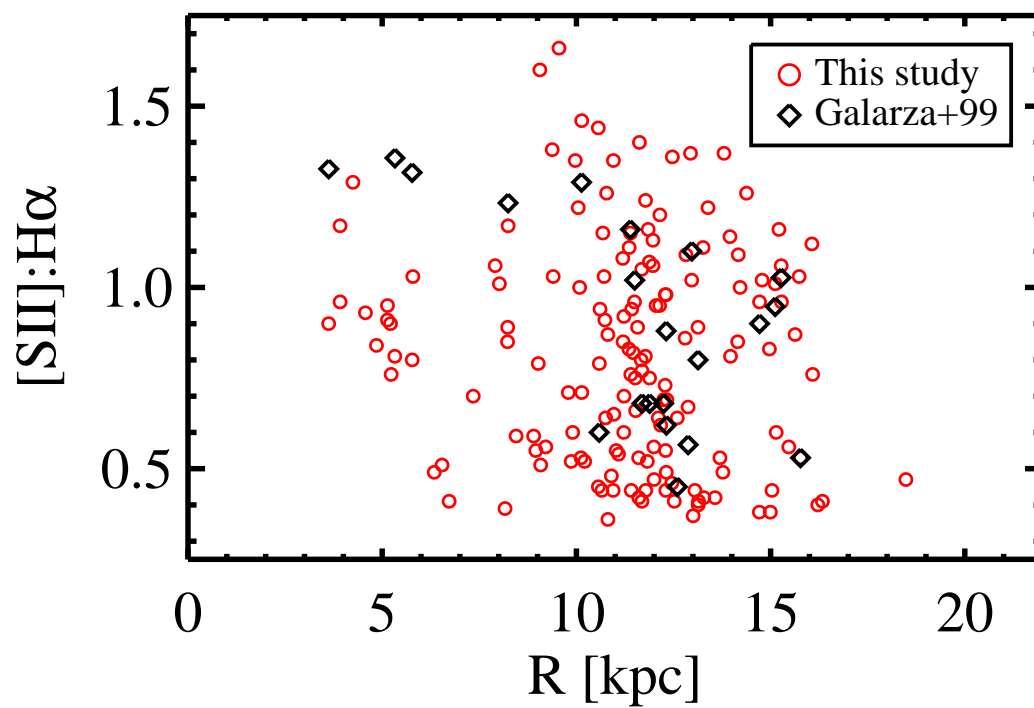


Fig. 14.— Comparison of radial distribution of [S II]:H α for M31 SNR candidates found in this study (circles) with that for SNR candidates derived from Galarza et al. (1999) (diamonds).

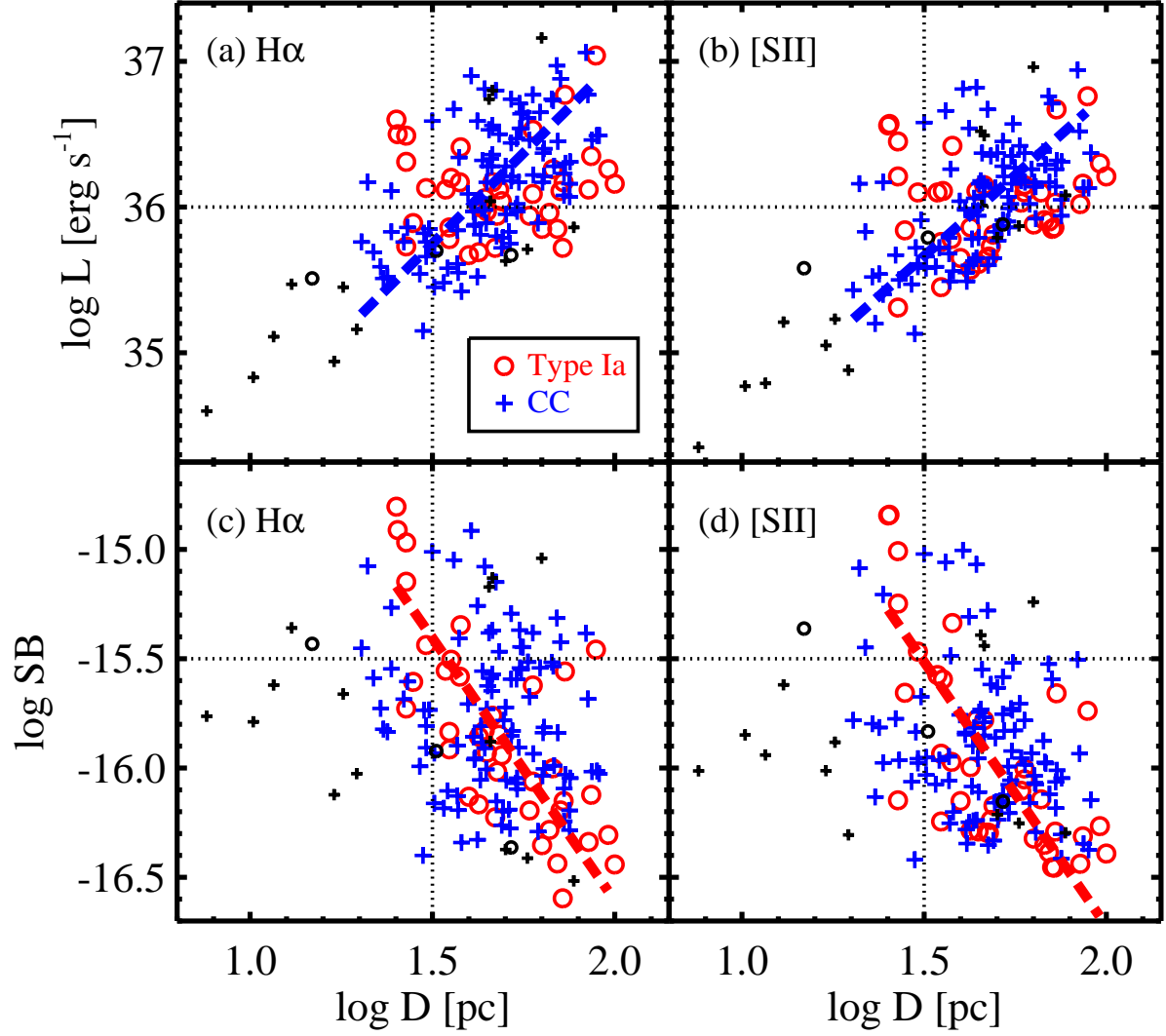


Fig. 15.— (Upper panels) Luminosity versus size and (lower panels) surface brightness versus size for Type Ia (circles) and CC (plus signs) SNR candidates in M31. Small symbols mark C-type SNR candidates. Thick lines represent linear least-squares fits.

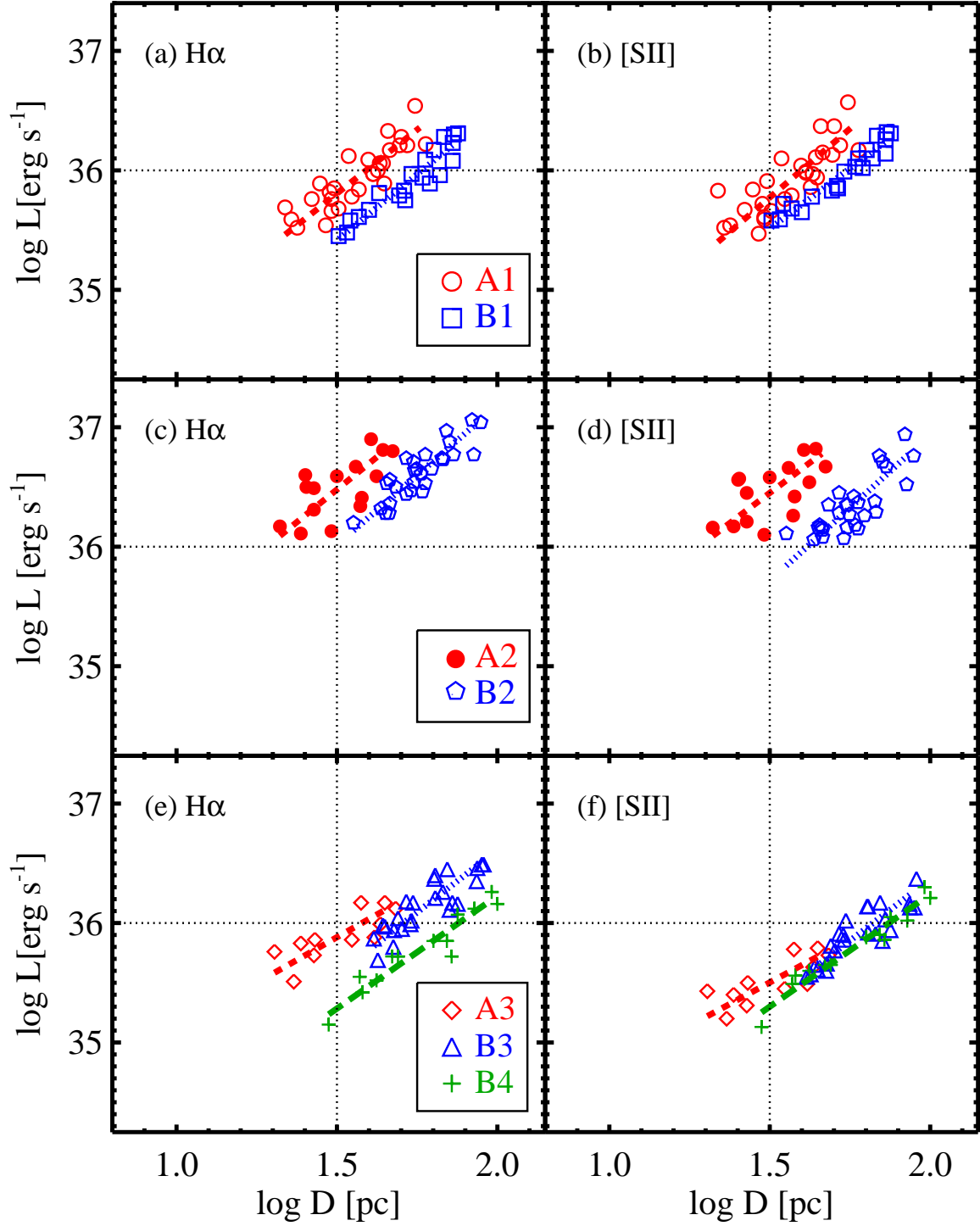


Fig. 16.— (Left panels) $\text{H}\alpha$ luminosity versus size for M31 SNR candidates of different morphological types: A1-type (open circles), B1-type (squares), A2-type (filled circles), B2-type (pentagons), A3-type (diamonds), B3-type (triangles), and B4-type (plus signs) SNR candidates. (Right panels) $[\text{S II}]$ luminosity versus size. Thick lines represent linear least-squares fits.

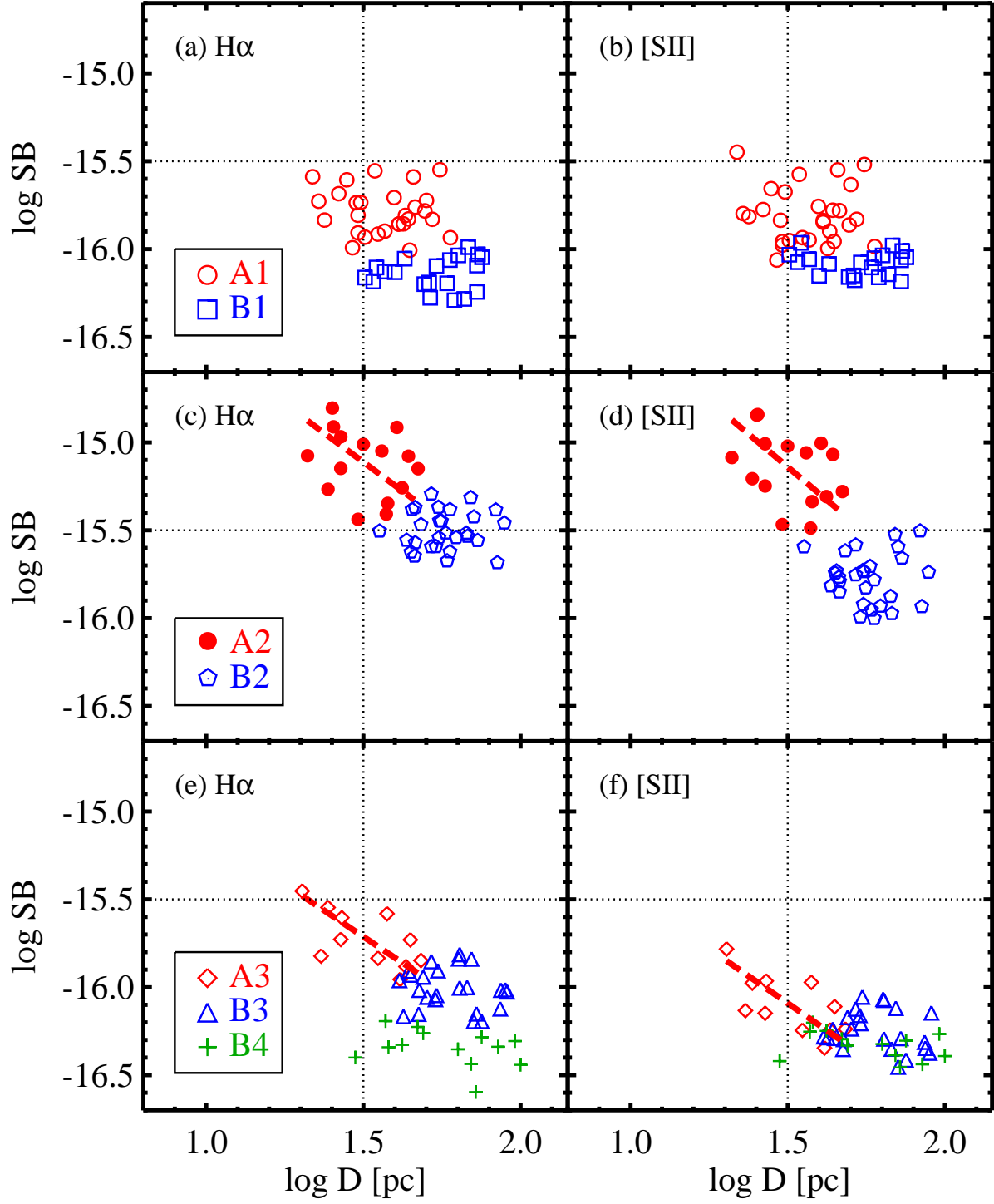


Fig. 17.— (Left panels) $H\alpha$ surface brightness versus size for M31 SNR candidates of different morphological types. (Right panels) $[S II]$ surface brightness versus size. Thick lines represent linear least-squares fits. Same symbols as in Figure 16.

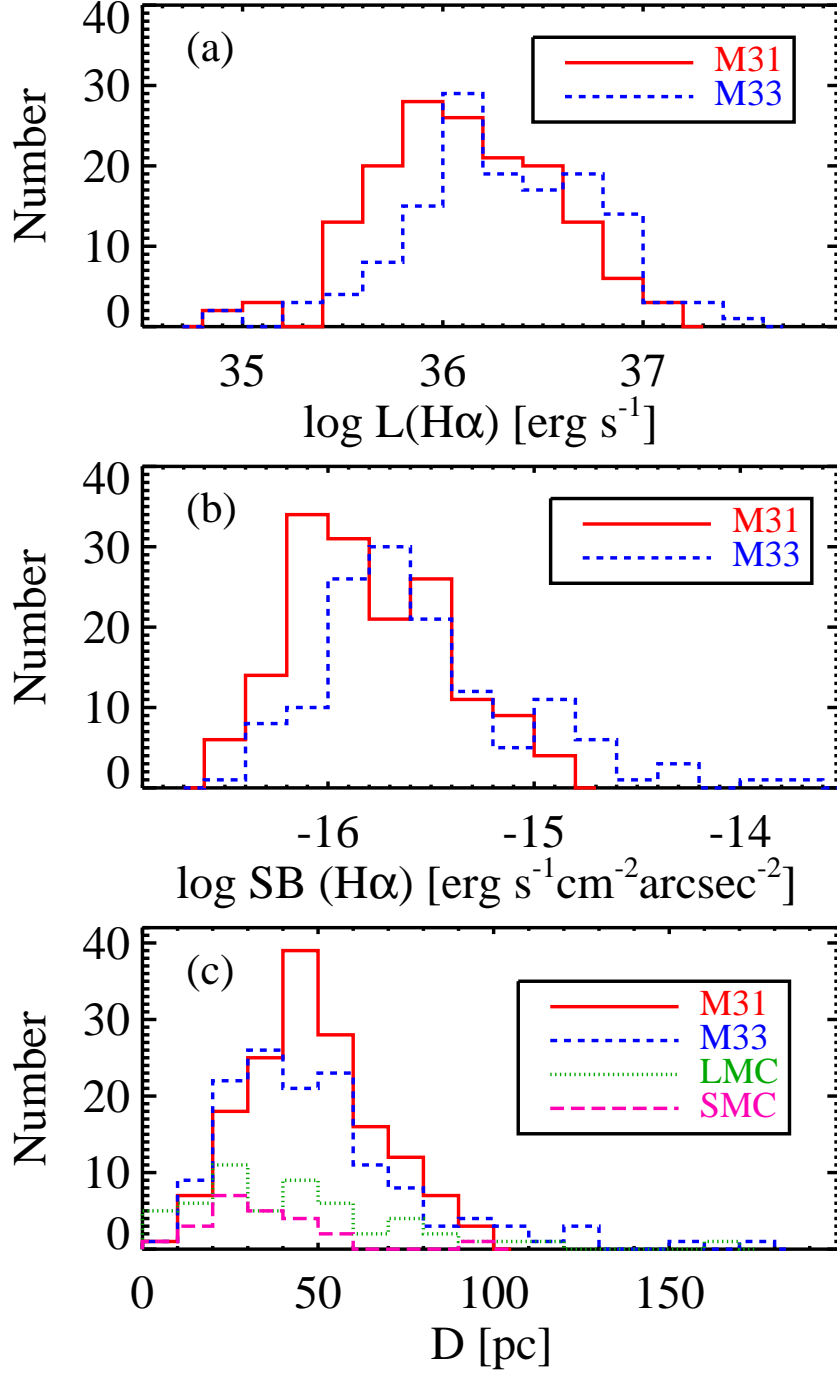


Fig. 18.— Comparisons of distributions of (a) $\text{H}\alpha$ luminosity, (b) $\text{H}\alpha$ surface brightness, and (c) size of SNR candidates in M31 (solid line), M33 [dashed line; Long et al. (2010)], the LMC [dotted line; Badenes et al. (2010)], and the SMC [long dashed line; Badenes et al. (2010)].

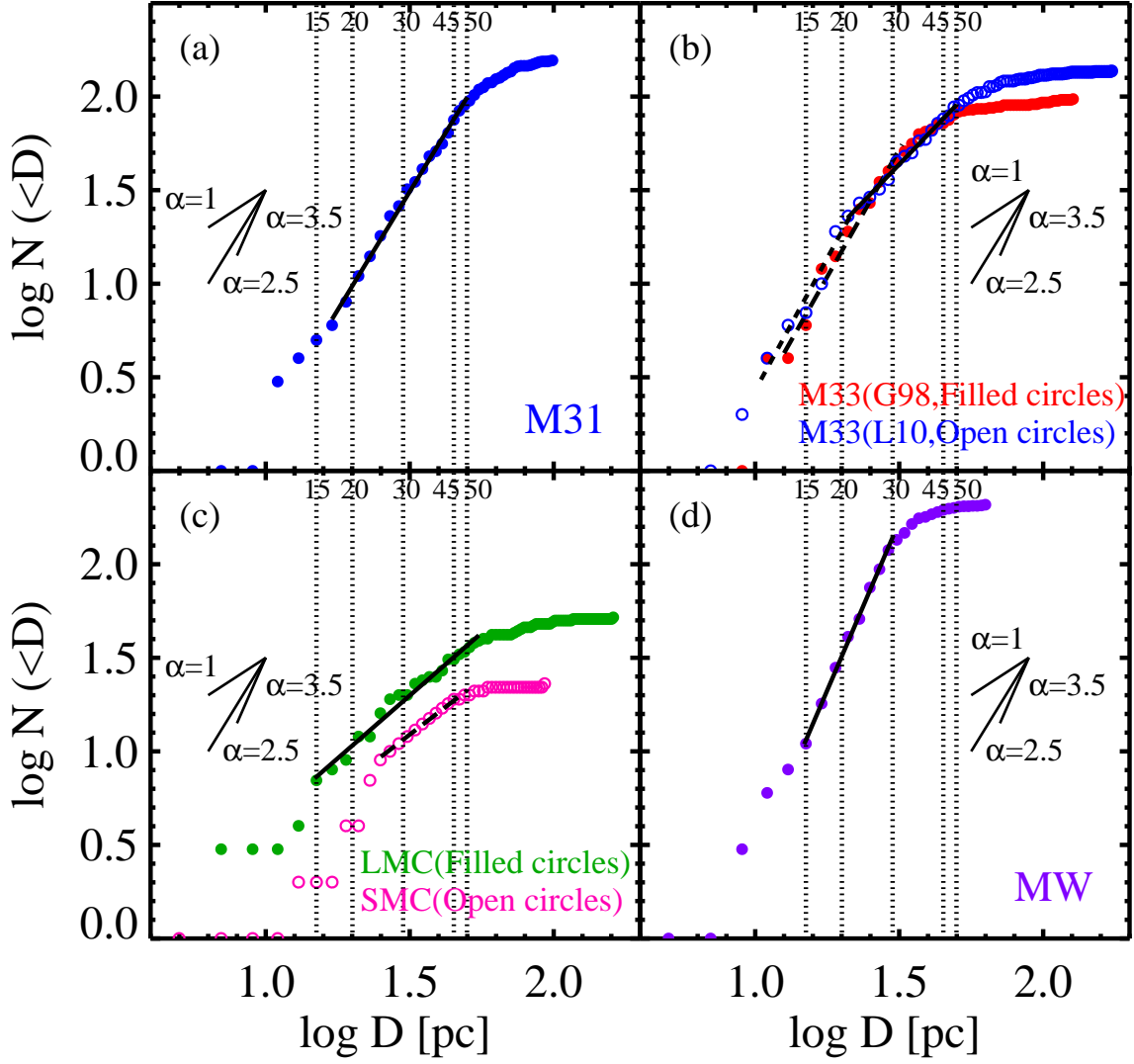


Fig. 19.— Comparisons of cumulative size distribution of SNR candidates in M31 (panel a) with those for M33 (panel b), the LMC (filled circles in panel c), the SMC (open circles in panel c), and the MW (panel d). SNR samples for M33, the MCs, and the MW are obtained from Gordon et al. (1998) and Long et al. (2010), Badenes et al. (2010), and Pavlović et al. (2013), respectively. Thick lines represent power law fits. The power law indices for the cumulative size distributions of SNR candidates in these galaxies are summarized in Table 6.

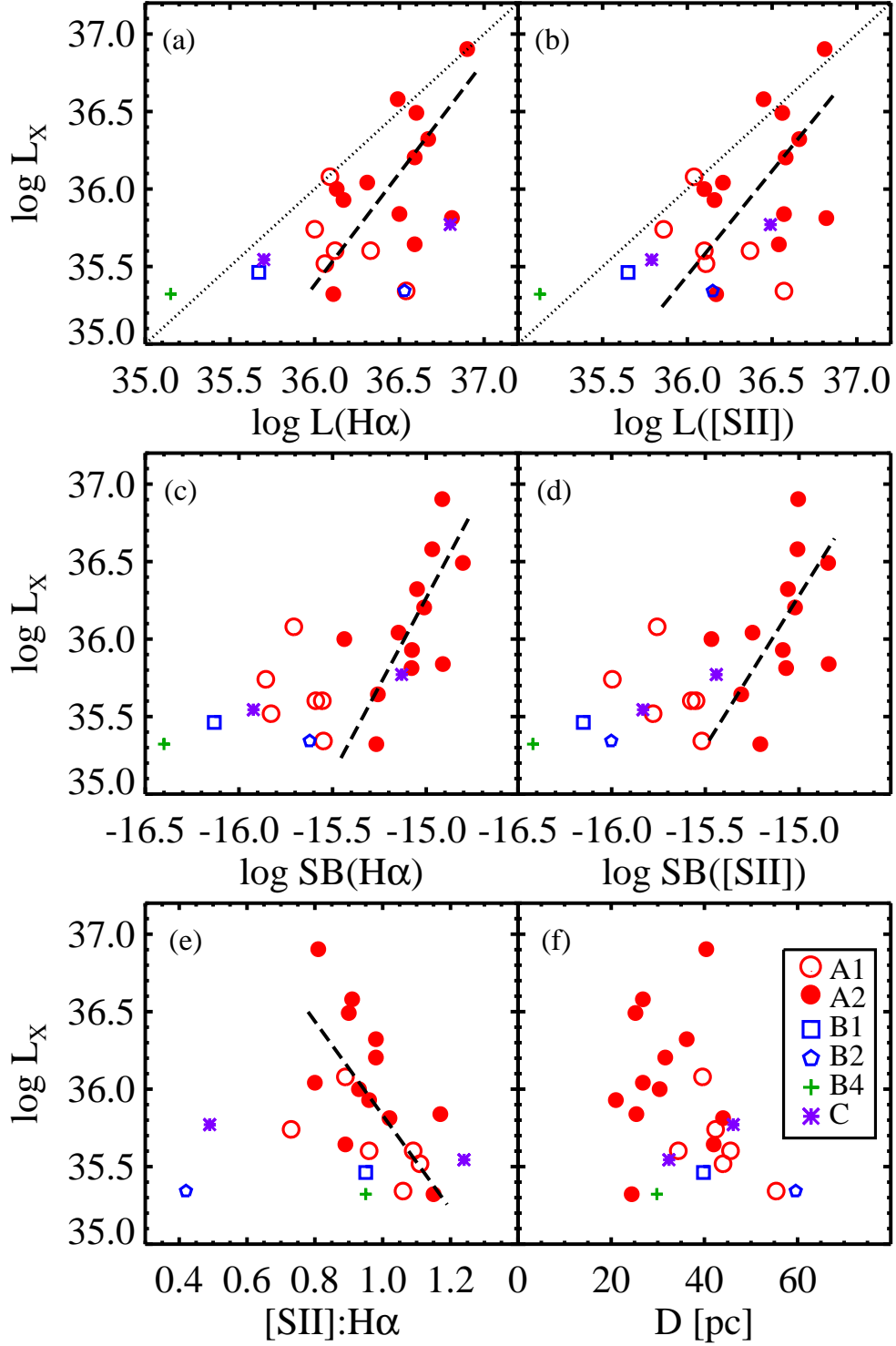


Fig. 20.— Comparisons of X-ray luminosity (L_x) and optical properties of M31 SNR candidates common to this study and Sasaki et al. (2012): (a) L_x versus $\text{H}\alpha$ luminosity, (b) L_x versus $[\text{S II}]$ luminosity, (c) L_x versus $\text{H}\alpha$ surface brightness, (d) L_x versus $[\text{S II}]$ surface brightness, (e) L_x versus $[\text{S II}]:\text{H}\alpha$, and (f) L_x versus size. Symbols in panels indicate morphological types of SNR candidates. Thick dashed lines in (a), (b), and (e) represent linear least-squares fits for the combined sample of A1-type and A2-type SNR candidates, and those in (c) and (d) represent fits for A2-type SNR candidates.

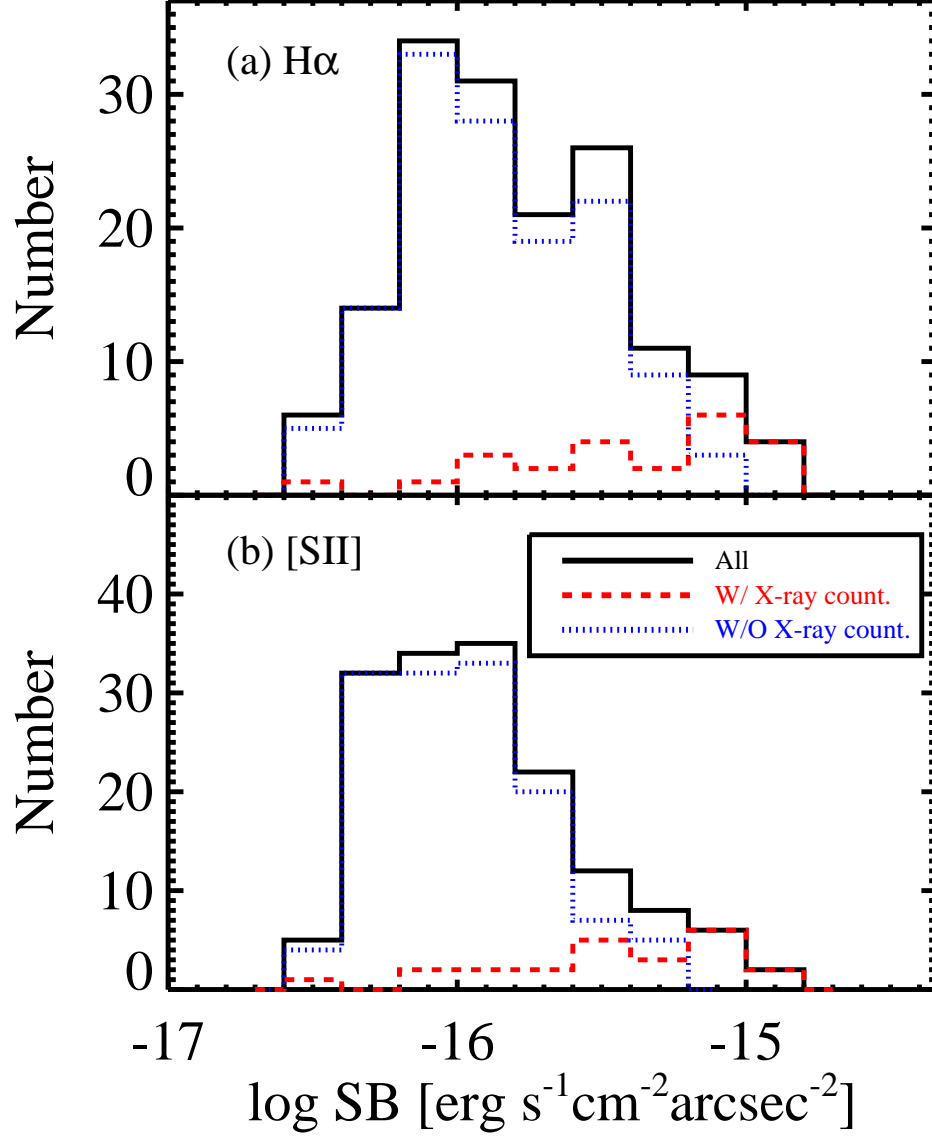


Fig. 21.— Distributions of (a) $\text{H}\alpha$ and (b) $[\text{S II}]$ surface brightness for SNR candidates with X-ray counterparts (dashed line), those without such counterparts (dotted line), and all SNR candidates (solid line) in M31.

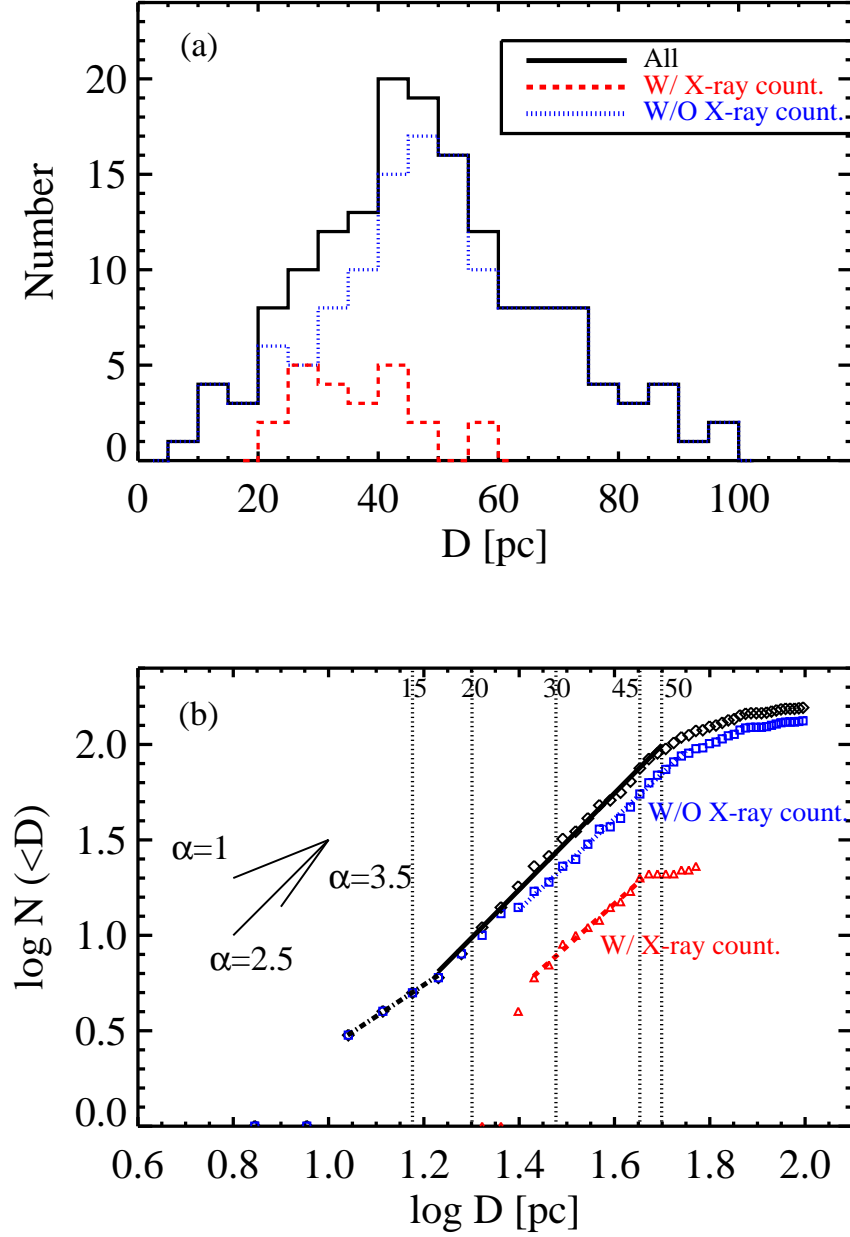


Fig. 22.— (a) Differential size distributions of SNR candidates with X-ray counterparts (dashed line), those without such counterparts (dotted line), and all SNR candidates (solid line) in M31. (b) Cumulative size distributions of SNR candidates with X-ray counterparts (triangles), those without such counterparts (squares), and all SNR candidates (diamonds) in M31. Thick lines represent power law fits. The power law index for SNR candidates with X-ray counterparts is $\alpha = 2.23 \pm 0.07$ (dotted line) for $27 \text{ pc} < D < 45 \text{ pc}$, which is similar to the value for SNR candidates without X-ray counterparts, $\alpha = 2.37 \pm 0.03$ (dashed line) for $25 \text{ pc} < D < 55 \text{ pc}$.

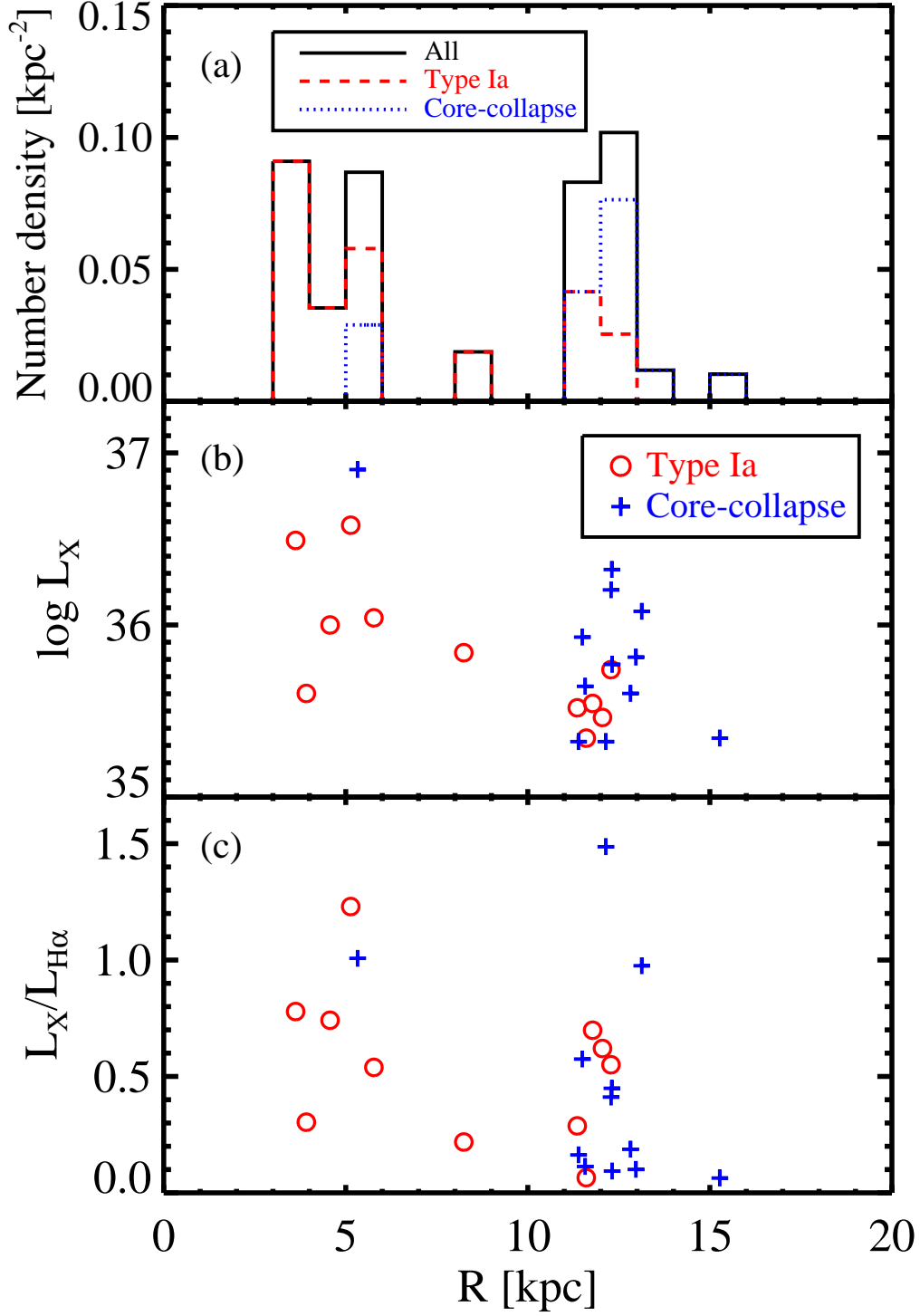


Fig. 23.— Radial distributions of (a) number density, (b) L_x , and (c) $L_x/L_{H\alpha}$ of all (solid line), Type Ia (dashed line, circles) and CC (dotted line, plus signs) SNR candidates with X-ray counterparts in M31.